Title	An enriched 6-node MITC plate element for yield line analysis
Author(s)	Xu, Jin; Lee, Chi King; Tan, Kang Hai
Citation	Xu, J., Lee, C. K., & Tan, K. H. (2013). An enriched 6-node MITC plate element for yield line analysis. Computers & Structures, 128, 64-76.
Date	2013
URL	http://hdl.handle.net/10220/18890
Rights	© 2013 Elsevier. This is the author created version of a work that has been peer reviewed and accepted for publication by Computers & Structures, Elsevier. It incorporates referee's comments but changes resulting from the publishing process, such as copyediting, structural formatting, may not be reflected in this document. The published version is available at: [DOI:http://dx.doi.org/10.1016/j.compstruc.2013.07.008].

Pre-printed version of the paper published in the journal: Computers and Structures, Vol. 128, pp64-76, 2013

A enriched 6-node XFEM MITC plate element for yield line analysis

Jin Xu[a, 1], C.K. Lee[a] and K.H. Tan[a]

School of Civil and Environmental Engineering, Nanyang Technological University,
Nanyang Avenue, Singapore 639798, Singapore
[1]xu0003in@e.ntu.edu.sg

Abstract

A 6-node triangular Reissner-Mindlin plate element with eXtended Finite Element Method (XFEM) formulation for yield line analyses is presented. The XFEM formulation with regularized enrichment is employed to reproduce a displacement field with a locally high gradient in the vicinity of a yield line in plate structures. The MITC technique is employed to mitigate shear locking in both the smooth and the locally non-smooth displacement fields. Several numerical examples are presented to illustrate the effectiveness of the XFEM enrichment in yield line analysis as well as the necessity and the effectiveness of the MITC technique in shear locking alleviation in the XFEM formulation.

Key words: MITC, XFEM, yield line analysis, regularized enrichment

1 Introduction

Shear locking is a major concern in developing a robust Reissner-Mindlin plate element [1]. It is well known that compatible plate elements behave too stiff when the ratio of thickness to length of the plate/shell structure approaches zero. The Mixed Interpolation of Tensorial Components (MITC) technique is an effective way to circumvent shear locking in plate elements [2-4] and shell elements [5-9]. In the MITC technique, an assumed strain field is employed instead of the compatible strain field derived from the displacement approximation. The unknown variables of the assumed strain field are evaluated by tying the assumed strain field and the compatible strain field at some selected points [10, 11]. Up to now, much efforts [12-17] have been devoted to improve the performance of the MITC elements. The MITC

technique has also been extended beyond FEM analysis: Nguyen et al [18] applied the MITC technique in the smoothed finite element method to alleviate shear locking for shell analysis. Carrera et al [19] adopted the MITC technique in Carrera Unified Formulation for the analysis of layered structures.

The application of the XFEM formulation in yield line analyses for plate structures has been presented in [20, 21]. as well as for the plastic mechanism analyses in beam structures [22]. The locally non-smooth displacement field resulted from a yield line can be reproduced by the XFEM formulation with regularized enrichment [23-27]. The regularized enrichment contains a locally non-smooth part, which is able to describe the displacement field inside a high gradient zone (HGZ). In general, when conducting a yield line analysis by the XFEM formulation, the location and the size of the non-smooth part is usually regarded as *a prior* knowledge. Relatively accurate results can be obtained by a coarse mesh and no additional mesh refinement technique is necessary during analyses. Hence a large amount of computational effort is saved. Different from the XFEM formulation with a real discontinuous enrichment [28-35], the XFEM formulation with a regularized enrichment expands the Ritz space of the numerical solution. Furthermore, the regularized enrichment is suppressed and activated *automatically* during an XFEM analysis. Therefore, the regularized enrichment could be included in the formulation at the initial stage of a nonlinear analysis and no specially designed criterion is needed to activate the enrichment during an analysis [20].

In this paper, a 6-node triangular C_0 plate element with the XFEM formulation aiming to model the non-smooth displacement approximation fields near a yield line is presented. The aim of the present XFEM formulation is to capture the elasto-plastic behavior of a plate by very few elements. The enrichments are constructed at the structure level and they exhibit a high gradient *normal* to the yield line but a zero gradient *along* the yield line. The rotation and the deflection approximation fields are enriched simultaneously by employing a regularized step function for rotation and a regularized level set function for deflection. The enrichments for the rotational displacement field are shifted so that the formulation is free from problems due to blending elements: the Partition of Unity (PU) condition can be satisfied over the whole physical domain naturally [32] and there is no unwanted strain term in blending elements [36]. The MITC6 scheme [9] is employed to alleviate the shear locking in the XFEM plate elements. It is noted that the MITC6 scheme is first proposed to be used with a 6-node triangular shell element, while a similar MITC7 scheme [4] is proposed for a

triangular plate element with quadratic displacement approximation field. However, the existence of an interior node with deflection DOF *only* makes the MITC7 plate element inconvenient to be adopted in the present XFEM formulation. Thus, the MITC6 scheme is selected instead of the MITC7 scheme, despite that the MITC7 scheme has a rigorous mathematic proof on its convergence [3] and performs better than the MITC6 scheme in pure bending cases [11].

In the next section, the MITC6 assumed transverse shear strain field and its alternative expressions which is specially developed to be used in conjunction with the XFEM plate element are presented. The enrichments for the rotation and the deflection displacements are then introduced in Section 3. They are then followed by the formulations of the XFEM plate elements. In Section 5, four examples are given to show the effectiveness of the XFEM enrichments proposed in yield line analysis and the MITC6 technique in shear locking control. The paper is then completed with conclusions and discussions.

2 The MITC technique and its alternative expressions

In the MITC technique, the assumed transverse shear strain field is constructed by the interpolation of compatible transverse shear strain at some selected tying points. Therefore, the relationship between the assumed shear strain components and the nodal displacement variables is only defined indirectly. In order to make the implementation of the MITC scheme more convenient in the XFEM formulation, a direct relationship between the assumed shear strain components and the nodal displacement variables is established as an alternative expression of the MITC6 scheme. It should be stressed that while such direct relationship does not present the tying points explicitly, the assumed transverse shear strain prescribed by the alternative expression is exactly the same as that by the original form.

2.1 The original form of the MITC6 scheme

In the original form of the MITC6 shell element, the assumed transverse shear strain field $\tilde{e}_{rt}$ and $\tilde{e}_{st}$ are expressed in terms of the element parent coordinate system *r*-*s*:

$$\tilde{e}_{rt} = a_1 + b_1 r + c_1 s + d_1 rs + e_1 r^2 + f_1 s^2 \tag{1}$$

$$\tilde{e}_{st} = a_2 + b_2 r + c_2 s + d_2 rs + e_2 r^2 + f_2 s^2 \tag{2}$$

where the coefficients a_1, a_2, b_1, … , f_2 are calculated from the compatible transverse shear strain components at the tying points shown in Fig. 1:

$$a_1 = \tilde{m}_{\mathrm{rt}}^1 - \tilde{l}_{\mathrm{rt}}^1,\ b_1 = 2\tilde{l}_{\mathrm{rt}}^1,\ e_1 = 0,$$

$$a_2 = \tilde{m}_{\mathrm{st}}^2 - \tilde{l}_{\mathrm{st}}^2,\ c_2 = 2\tilde{l}_{\mathrm{st}}^2,\ f_2 = 0,$$

$$c_1 = 6e_{\mathrm{crt}} - 3e_{\mathrm{cst}} + 2\tilde{m}_{\mathrm{st}}^3 - 2\tilde{m}_{\mathrm{rt}}^3 - 4a_1 - b_1 + a_2,$$

$$b_2 = -3e_{\mathrm{crt}} + 6e_{\mathrm{cst}} - 2\tilde{m}_{\mathrm{st}}^3 + 2\tilde{m}_{\mathrm{rt}}^3 + a_1 - 4a_2 - c_2,$$

$$e_2 = 3e_{\mathrm{crt}} - 6e_{\mathrm{cst}} + 3\tilde{m}_{\mathrm{st}}^3 - \tilde{l}_{\mathrm{st}}^3 - 3\tilde{m}_{\mathrm{rt}}^3 + \tilde{l}_{\mathrm{rt}}^3 + b_1 + 3a_2 + c_2,$$

$$f_1 = -6e_{\mathrm{crt}} + 3e_{\mathrm{cst}} - 3\tilde{m}_{\mathrm{st}}^3 - \tilde{l}_{\mathrm{st}}^3 + 3\tilde{m}_{\mathrm{rt}}^3 + \tilde{l}_{\mathrm{rt}}^3 + 3a_1 + b_1 + c_2,$$

$$d_1 = -e_2,\ d_2 = -f_1$$

and

$$\tilde{m}_{j\mathrm{t}}^i = \frac{1}{2}\left(e_{1\,j\mathrm{t}}^i + e_{2\,j\mathrm{t}}^i\right),\ \tilde{l}_{j\mathrm{t}}^i = \frac{\sqrt{3}}{2}\left(e_{2\,j\mathrm{t}}^i - e_{1\,j\mathrm{t}}^i\right)$$

with $j = r, s$ and $i = 1, 2, 3$. In Fig. 1, $r_1 = s_1 = \frac{1}{2} - \frac{1}{2\sqrt{3}}$, $r_2 = s_2 = \frac{1}{2} + \frac{1}{2\sqrt{3}}$ and $r_3 = s_3 = \frac{1}{3}$.

2.2 The alternative form of the MITC6 scheme

In the present paper, an alternative expression of the assumed transverse shear strain field for the MITC6 scheme is derived. By substituting the natural coordinates of the tying points into Eqns. (1) and (2), the alternative expression can be written as:

$$\tilde{e}_{\mathrm{rt}} = -h_{\mathrm{rr}i}\beta_{\mathrm{r}i} - h_{\mathrm{rs}}\beta_{\mathrm{s}i} + h_{\mathrm{rw}\,i}w_i \tag{3}$$

$$\tilde{e}_{\mathrm{st}} = -h_{\mathrm{sr}i}\beta_{\mathrm{r}i} - h_{\mathrm{ss}}\beta_{\mathrm{s}i} + h_{\mathrm{sw}\,i}w_i \tag{4}$$

where w_i is the nodal deflection, $\beta_{\mathrm{r}i}$ and $\beta_{\mathrm{s}i}$ are the nodal rotation angles of the lines normal to the undeformed neutral surface in the r-t and s-t planes, respectively (Fig. 2). $h_{\mathrm{rr}i}$ and $h_{\mathrm{rs}i}$ are the interpolation functions for the assumed shear strain $\tilde{e}_{\mathrm{rt}}$ corresponding to $\beta_{\mathrm{r}i}$ and $\beta_{\mathrm{s}i}$, respectively. Finally, $h_{\mathrm{sr}i}$ and $h_{\mathrm{ss}i}$ are the interpolation functions for the assumed shear strain $\tilde{e}_{\mathrm{st}}$ corresponding to $\beta_{\mathrm{r}i}$ and $\beta_{\mathrm{s}i}$, respectively.

From Eqns. (3) and (4) it can be seen that, different from the compatible strain field, the assumed shear strain $\tilde{e}_{\mathrm{rt}}$ not only depends on the rotation $\beta_{\mathrm{r}i}$ and the deflection w_i, but also depends on the rotation $\beta_{\mathrm{s}i}$. Similar observation can be found for the assumed shear strain $\tilde{e}_{\mathrm{st}}$. This contribution comes from the two tying points on the hypotenuse edge and the tying point at the center of the triangular element (Fig. 1a). It can be seen that the alternative expression can be written in terms of an interpolation of the nodal displacement variables.

The interpolation functions $h_{\mathrm{rr}i}$, $h_{\mathrm{rs}i}$, $h_{\mathrm{sr}i}$ and $h_{\mathrm{ss}i}$ are obtained by substituting the natural coordinates into the coefficients $a_1, a_2, b_1, \ldots, f_2$ in Eqns. (1) and (2). After simplification, the interpolation functions are written as:

$$h_{\mathrm{rr}1}=\frac{2}{3}-r-\frac{7}{3}s+\frac{4}{3}rs+\frac{5}{3}s^2,\ h_{\mathrm{rr}2}=-\frac{1}{3}+r-\frac{2}{3}s+\frac{1}{3}rs+\frac{2}{3}s^2,\ h_{\mathrm{rr}3}=-s+\frac{1}{3}rs+\frac{5}{3}s^2,$$

$$h_{\mathrm{rr}4}=\frac{2}{3}-\frac{4}{3}rs-\frac{2}{3}s^2,\ h_{\mathrm{rr}5}=\frac{4}{3}s+\frac{2}{3}rs-\frac{2}{3}s^2,\ h_{\mathrm{rr}6}=\frac{8}{3}s-\frac{4}{3}rs-\frac{8}{3}s^2 \tag{5}$$

$$h_{\mathrm{rs}1}=s-\frac{5}{3}rs-\frac{4}{3}s^2,\ h_{\mathrm{rs}2}=\frac{2}{3}s-\frac{5}{3}rs-\frac{1}{3}s^2,\ h_{\mathrm{rs}3}=\frac{1}{3}s-\frac{2}{3}rs-\frac{1}{3}s^2,$$

$$h_{\mathrm{rs}4}=-\frac{4}{3}s+\frac{8}{3}rs+\frac{4}{3}s^2,\ h_{\mathrm{rs}5}=\frac{2}{3}rs-\frac{2}{3}s^2,\ h_{\mathrm{rs}6}=-\frac{2}{3}s+\frac{2}{3}rs+\frac{4}{3}s^2 \tag{6}$$

$$h_{\mathrm{sr}1}=r-\frac{5}{3}rs-\frac{4}{3}r^2,\ h_{\mathrm{sr}2}=\frac{1}{3}r-\frac{2}{3}rs-\frac{1}{3}r^2,\ h_{\mathrm{sr}3}=\frac{2}{3}r-\frac{5}{3}rs-\frac{1}{3}r^2,$$

$$h_{\mathrm{sr}4}=-\frac{2}{3}r-\frac{5}{3}rs-\frac{1}{3}r^2,\ h_{\mathrm{sr}5}=\frac{2}{3}rs-\frac{2}{3}r^2,\ h_{\mathrm{sr}6}=-\frac{4}{3}r+\frac{8}{3}rs+\frac{4}{3}r^2 \tag{7}$$

$$h_{\mathrm{ss}1}=\frac{2}{3}-\frac{7}{3}r-s+\frac{4}{3}rs+\frac{5}{3}r^2,\ h_{\mathrm{ss}2}=-r+\frac{1}{3}rs+\frac{5}{3}r^2,\ h_{\mathrm{ss}3}=-\frac{1}{3}-\frac{2}{3}r+s+\frac{1}{3}rs+\frac{2}{3}r^2$$

$$h_{\mathrm{ss}4}=\frac{8}{3}r-\frac{4}{3}rs-\frac{8}{s}r^2,\ h_{\mathrm{ss}5}=\frac{4}{3}r+\frac{2}{3}rs-\frac{2}{3}r^2,\ h_{\mathrm{ss}6}=\frac{2}{3}-\frac{4}{3}rs-\frac{2}{3}r^2 \tag{8}$$

$$h_{\mathrm{rw}i}=\frac{\partial N_i}{\partial r},\ h_{\mathrm{sw}i}=\frac{\partial N_i}{\partial s} \tag{9}$$

where N_i are the standard shape functions for a 6-node triangular element.

3 The XFEM enrichment functions

For a plate structure, non-smoothness often appears locally in displacement fields in the vicinity of a yield line. Different from a *real* discontinuity such as a crack in a plate, this non-smoothness is formed within a finite range which is *not* zero in width, but with a finite width l_{ns}. Such non-smoothness is associated with the term 'high gradient' [37], and the region with the locally non-smooth displacement is often referred as the high gradient zone.

In the present XFEM formulation, both of the rotation and the deflection displacement fields are enriched. The enrichments for the rotation and the deflection displacements field are at least C_1 continuous over the whole physical domain. Furthermore, the enrichment for the rotation is a function in which its *value* changes sign sharply along the direction of the yield line, while the enrichment for the deflection field is a function in which its *gradient* changes sign within a short range. Besides, the variation of rotation displacement and the gradient of deflection displacement along the yield line direction are smooth. Hence, in the present formulation, the *ridge functions* are used in both the rotation and deflection fields.

In the present XFEM plate element, a high gradient zone is defined at the structure level by a level set function, $\varphi(x, y) = 0$ and width l_{ns}. An example of a HGZ with $\varphi = 3x - 2y + 8 = 0$ and $l_{\text{ns}} = 1.5$ in a square domain $(x, y) \in [0, 10] \times [0, 10]$ is shown in Fig. 3.

The enrichment function S for the rotation approximation field is expressed by

$$S_i(\varphi) = R(\varphi) - H(\varphi_i) \tag{10}$$

where $R(\varphi)$ is the regularized enrichment function for the *rotation displacement* approximation field before shifting, which can be expressed as [21]

$$R = \begin{cases} -1 & \varphi < -0.5l_{\text{ns}} \\ \dfrac{3}{l_{\text{ns}}}\varphi - \dfrac{4}{l_{\text{ns}}^3}\varphi^3 & -0.5l_{\text{ns}} \le \varphi \le 0.5l_{\text{ns}} \\ 1 & \varphi \ge 0.5l_{\text{ns}} \end{cases} \tag{11}$$

In Eqn. (10), $H(\varphi_i)$ ($i = 1, 2, \ldots, n_{\text{node}}$) is the nodal value of the Heaviside function at node i.

$$H(\varphi) = \begin{cases} 1 & \varphi > 0 \\ 0 & \varphi = 0 \\ -1 & \varphi < 0 \end{cases} \tag{12}$$

A plot of $R(\varphi)$ and its first derivative with respect to the global coordinates corresponding to the particular case of $\varphi = 3x - 2y + 8 = 0$ and $l_{ns} = 1.5$ is shown in Fig. 4. Since the enrichment is shifted, the enrichment function S_i is non-zero within the domain of enriched elements only. Therefore, the problems due to blending elements, namely the violation of the PU condition and the unwanted strain terms appearing in blend elements [38] are eliminated in the rotation displacement approximation field [36].

The enrichment function F for the *deflection displacement* approximation field used in the present formulation is of the form

$$F(\varphi) = \begin{cases} 1.0 - \dfrac{8}{l_{ns}^{\,2}}\varphi^2 + \dfrac{16}{l_{ns}^{\,4}}\varphi^4 & |\varphi| < 0.5 l_{ns} \\ 0 & \text{otherwise} \end{cases} \tag{13}$$

A plot of $F(\varphi)$ and its first derivative with respect to the global coordinates corresponding to the particular case of $\varphi = 3x - 2y + 8 = 0$ and $l_{ns} = 1.5$ is shown in Fig. 5. It can be seen that the $F(\varphi)$ is already suppressed to zero outside the high gradient zone. Therefore, it is unnecessary to apply shift technique for the enrichment function $F(\varphi)$.

Different from the enrichment functions presented in [20], the enrichment functions in this study are constructed based on the global coordinates and independent of the standard finite element shape functions. This approach results in the advantage that the present enrichment functions are invariant under different mesh schemes. As a result, the enrichment functions can be used in a distorted mesh scheme. A disadvantage of the present enrichment function is that the result from the present XFEM formulation depends on the size of enriched elements, which is also reported in [39]. The source of the dependence is shown in Section 4.2.

As the high gradient zone forms gradually during the yielding process, it is hard to identify when the HGZ comes into existence in an elasto-plastic analysis. In the present formulation, the enrichment is added into the formulation at the *beginning* of the analysis. Since the addition of regularized enrichment is equivalent to enlarge the Ritz space of the numerical solution, the enrichment will be activated according to the necessity of the analysis automatically [20, 21].

4 Formulations for the XFEM plate elements

4.1 The degrees of freedom and displacement approximation field

It is assumed that the plate element is initially flat and placed in the x-y plane. For an enriched element, there are six degrees of freedom (DOF) per node, which is denoted as $\mathbf{u}_{\mathrm{enr}i} = (w_i, \theta_{\mathrm{x}i}, \theta_{\mathrm{y}i}, a_{\mathrm{x}i}, a_{\mathrm{y}i}, b_i)^{\mathrm{T}}$, ($i$ =1, 2, …, 6). As shown in Fig. 6, w_i is the out-of-plane deflection at node i and $\theta_{\mathrm{x}i}$ and $\theta_{\mathrm{y}i}$ are the rotational angle with respect to x- and y-axis, respectively. The variables $a_{\mathrm{x}i}$ and $a_{\mathrm{y}i}$ are the enriched (non-smooth) rotation DOF with respective to the x- and y-axis whereas b_i is the enriched (non-smooth) deflection DOF.

The deflection field w_{h} and rotation field θ_{xh} and θ_{yh} are approximated by the sum of the *smooth part* and the *non-smooth part*:

$$\begin{pmatrix} w_{\mathrm{h}} \\ \theta_{\mathrm{xh}} \\ \theta_{\mathrm{yh}} \end{pmatrix} = \sum_{i=1}^{6} N_i \begin{pmatrix} w_i \\ \theta_{\mathrm{x}i} \\ \theta_{\mathrm{y}i} \end{pmatrix} + \sum_{i=1}^{6} N_i \begin{pmatrix} Fb_i \\ S_i a_{\mathrm{x}i} \\ S_i a_{\mathrm{y}i} \end{pmatrix} \tag{14}$$

where F (Eqn. (10)) and S_i (Eqn. (13)) are the enrichments for the non-smooth deflection and rotation displacement, respectively. In a small deformation analysis, the rotation DOF can be regarded as a vector as the translational DOF [40] so that the rotation DOF $\theta_{\mathrm{x}i}$, $\theta_{\mathrm{y}i}$ and the additional DOF, $a_{\mathrm{x}i}$ and $a_{\mathrm{y}i}$, can be added together.

4.2 The kinematic equation

A layered model, as shown in Fig. 7, is adopted in the present XFEM plate element so that the elasto-plastic behavior of a plate structure can be traced. The middle surface of an element is selected as the reference surface. The bending strain of the j^{th} layer $\boldsymbol{\varepsilon}_{\mathrm{b}j}$ can be expressed as

$$\boldsymbol{\varepsilon}_{\mathrm{b}j} = -z_j \boldsymbol{\chi} \tag{15}$$

where z_j is the distance between the reference surface and the middle surface of the j^{th} layer. $\boldsymbol{\chi}$ is the curvature:

$$\boldsymbol{\chi}=\begin{pmatrix}\sum_{i=1}^{6}\frac{\partial N_i}{\partial x}\beta_{\mathrm{x}i}\\ \sum_{i=1}^{6}\frac{\partial N_i}{\partial y}\beta_{\mathrm{y}i}\\ \sum_{i=1}^{6}\frac{\partial N_i}{\partial x}\beta_{\mathrm{y}i}+\sum_{i=1}^{6}\frac{\partial N_i}{\partial y}\beta_{\mathrm{x}i}\end{pmatrix}+\begin{pmatrix}\sum_{i=1}^{6}\frac{\partial\left(N_iS_i\right)}{\partial x}\alpha_{\mathrm{x}i}\\ \sum_{i=1}^{6}\frac{\partial\left(N_iS_i\right)}{\partial y}\alpha_{\mathrm{y}i}\\ \sum_{i=1}^{6}\frac{\partial\left(N_iS_i\right)}{\partial x}\alpha_{\mathrm{y}i}+\sum_{i=1}^{6}\frac{\partial\left(N_iS_i\right)}{\partial y}\alpha_{\mathrm{x}i}\end{pmatrix} \tag{16}$$

where α_{x} and α_{y} are the non-smooth rotation angles of the lines normal to the undeformed neutral surface in the x-z and y-z planes. β_{x} and β_{y} are the smooth rotation angles of the lines normal to the undeformed neutral surface in the x-z and y-z planes.

The assumed transverse shear strain can be expressed as

$$\tilde{\mathbf{e}}=\begin{pmatrix}\tilde{e}_{\mathrm{rt}}\\ \tilde{e}_{\mathrm{st}}\end{pmatrix}=\begin{pmatrix}-h_{\mathrm{rr}i}\beta_{\mathrm{r}i}-h_{\mathrm{rr}i}S_i\alpha_{\mathrm{r}i}-h_{\mathrm{rs}i}\beta_{\mathrm{s}i}-h_{\mathrm{rs}i}S_i\alpha_{\mathrm{s}i}+h_{\mathrm{rw}i}w_i+h_{\mathrm{rb}i}b_i\\ -h_{\mathrm{sr}i}\beta_{\mathrm{r}i}-h_{\mathrm{sr}i}S_i\alpha_{\mathrm{r}i}-h_{\mathrm{ss}i}\beta_{\mathrm{s}i}-h_{\mathrm{ss}i}S_i\alpha_{\mathrm{s}i}+h_{\mathrm{sw}i}w_i+h_{\mathrm{sb}i}b_i\end{pmatrix} \tag{17}$$

where the interpolation functions $h_{\mathrm{rr}i}$, $h_{\mathrm{rs}i}$, $h_{\mathrm{rw}i}$, $h_{\mathrm{sr}i}$, $h_{\mathrm{ss}i}$ and $h_{\mathrm{sw}i}$ are expressed in Eqns. (5) − (9), respectively. Note that the assumed shear strains are also employed for the enriched part. $h_{\mathrm{rb}i}$ and $h_{\mathrm{sb}i}$ are the interpolation functions corresponding to b_i and they can be expressed explicitly as

$$h_{\mathrm{rb}i}=\frac{\partial N_i}{\partial r}F+N_i\frac{\partial F}{\partial r} \tag{18}$$

$$h_{\mathrm{sb}i}=\frac{\partial N_i}{\partial s}F+N_i\frac{\partial F}{\partial s} \tag{19}$$

In Eqn. (17), β_{r} and β_{s}, as shown in Fig. 6, are the rotation angles of the lines normal to the undeformed neutral surface in the *r*-*t* and *s*-*t* planes, respectively, which can be written in matrix form as [41]

$$\begin{pmatrix}\beta_{\mathrm{r}}\\ \beta_{\mathrm{s}}\end{pmatrix}=\begin{bmatrix}0 & -1\\ 1 & 0\end{bmatrix}\begin{pmatrix}\theta_{\mathrm{r}}\\ \theta_{\mathrm{s}}\end{pmatrix} \tag{20}$$

α_{r} and α_{s}, as shown in Fig. 6 again, are the rotation angles of the lines normal to the undeformed reference surface in the *r*-*t* and *s*-*t* plane due to the non-smooth rotation:

$$\begin{pmatrix}\alpha_{\mathrm{r}}\\ \alpha_{\mathrm{s}}\end{pmatrix}=\begin{bmatrix}0 & -1\\ 1 & 0\end{bmatrix}\begin{pmatrix}a_{\mathrm{r}}\\ a_{\mathrm{s}}\end{pmatrix} \tag{21}$$

In Eqns. (16), (18) and (19), the first derivative of the enrichments, S_i and F, with respect to the natural coordinates r and s is of the form

$$\frac{\partial S_i}{\partial \mathbf{r}^{\mathrm{T}}} = \frac{\partial \mathbf{x}}{\partial \mathbf{r}^{\mathrm{T}}} \frac{\partial \varphi}{\partial \mathbf{x}^{\mathrm{T}}} \frac{\partial R}{\partial \varphi} \Big/ \left| \frac{\partial \varphi}{\partial \mathbf{x}} \right| \tag{22}$$

$$\frac{\partial F}{\partial \mathbf{r}^{\mathrm{T}}} = \frac{\partial \mathbf{x}}{\partial \mathbf{r}^{\mathrm{T}}} \frac{\partial \varphi}{\partial \mathbf{x}^{\mathrm{T}}} \frac{\partial F}{\partial \varphi} \Big/ \left| \frac{\partial \varphi}{\partial \mathbf{x}} \right| \tag{23}$$

where $\partial\varphi/\partial\mathbf{x}^{\mathrm{T}}$ is the direction vector of φ, $\mathbf{x}=(x, y)^{\mathrm{T}}$ and $\partial/\partial\mathbf{r}^{\mathrm{T}}=(\partial/\partial r, \partial/\partial s)^{\mathrm{T}}$. As the value of $\partial S_i/\partial\mathbf{r}^{\mathrm{T}}$ and $\partial F/\partial\mathbf{r}^{\mathrm{T}}$ depends on $\partial\mathbf{x}/\partial\mathbf{r}^{\mathrm{T}}$, the entries in the stiffness matrix corresponding to the additional DOF are mesh size sensitive.

In order to show the necessity of the application of the MITC technique in shear strain corresponding to the smooth and the non-smooth displacement field, the following two schemes are also used in this paper, which are expressed as

$$\boldsymbol{\gamma}_{\mathrm{ScEa}} = \begin{pmatrix} -N_i\beta_{\mathrm{r}i} - h_{\mathrm{rr}i}S\alpha_{\mathrm{r}i} - h_{\mathrm{rs}i}S\alpha_{\mathrm{s}i} + h_{\mathrm{rw}i}w_i + h_{\mathrm{rb}i}b_i \\ -N_i\beta_{\mathrm{r}i} - h_{\mathrm{sr}i}S\alpha_{\mathrm{r}i} - h_{\mathrm{ss}i}S\alpha_{\mathrm{s}i} + h_{\mathrm{sw}i}w_i + h_{\mathrm{sb}i}b_i \end{pmatrix} \tag{24}$$

and

$$\boldsymbol{\gamma}_{\mathrm{SaEc}} = \begin{pmatrix} -h_{\mathrm{rr}i}\beta_{\mathrm{r}i} - N_iS\alpha_{\mathrm{r}i} - h_{\mathrm{rs}i}\beta_{\mathrm{s}i} + h_{\mathrm{rw}i}w_i + h_{\mathrm{rb}i}b_i \\ -h_{\mathrm{sr}i}\beta_{\mathrm{r}i} - h_{\mathrm{ss}i}\beta_{\mathrm{s}i} - N_iS\alpha_{\mathrm{s}i} + h_{\mathrm{sw}i}w_i + h_{\mathrm{sb}i}b_i \end{pmatrix} \tag{25}$$

On the left hand side of Eqns. (24) and (25), the subscript 'S' refers to the shear strain corresponding to the standard displacement field, 'E' refers to the shear strain corresponding to the enriched field, 'c' refers to 'compatible' and 'a' refers to 'assumed'. Therefore, Eqn. (24) expresses a shear strain field with the MITC technique applied on the ~~**standard**~~ **enriched?** displacement only, while (25) provides a shear strain field with the MITC technique applied on the ~~**enriched**~~ **standard?** displacement only. **{XJ: It seems that you mixed up Eqns. 24 and 25? Check!}**

The von-Mises yield criterion for plane stress is employed in the present element. A backward Euler return algorithm [42] is adopted to 'pull' a stress state back onto the yield surface. As the yield criterion is applied at the target stress state, a nonlinear equation is established in which plastic multiplier is the only unknown variable. In order to solve the nonlinear equation, Newton iteration is conducted.

4.3 The partition of enriched element

As shown in Fig. 8, a high gradient zone could cut through an enriched element in several different possibilities in the present formulation. In Fig. 8, 'TR', 'QU' and 'PE' refer to a triangular, a quadrilateral and a pentagon area, while 'H' refers to a high gradient zone (the shaded area) and 'nH' refers to a non-high gradient zone (the blank area). When a pentagon area appears in the partition (Fig. 8e), it is further divided into two quadrilateral area.

The 6 × 6 Gaussian integration scheme is employed in each area. As the order of strain term is up to 5, therefore the 6 × 6 Gaussian integration scheme is sufficient to integrate terms appear in stiffness matrix accurately. On the other hand, there are 36 (6 × 6) DOFs in an enriched element, and the 6 × 6 Gaussian integration scheme is able to provide 180 (6 × 6 × 5) independent relationships for the stiffness matrix of an enriched element. Hence, the singularity of the stiffness matrix can be prevented even if the entire element is occupied by a high gradient zone (Fig. 8d).

5 Numerical examples

In this section, four examples are presented to illustrate the robustness of the application of the MITC technique in the proposed XFEM formulation as well as the effectiveness of the XFEM formulation in capturing the behavior of plate structures in yield line analyses. In order to show the necessity of the employment of the MITC technique in the XFEM formulation, analysis with the compatible XFEM formulation is also carried out for each example. In each plate bending example, several cases with different thickness of the plates are tested. The yield strength and the external loading are adjusted accordingly to the plate thickness so that the ultimate loading levels are the same for each case. Since the main objective to formulate the XFEM plate element is to capture the behavior of the plate structure with as few elements as possible, in all the examples, only very coarse meshes with a few XFEM elements are used and no refinement study is carried out. Furthermore, since the enrichment is constructed at the structure level, the mesh size could influence the partial derivative of the enrichment function (Eqns. (22) and (23)). Therefore, the numerical result is influenced by mesh size of a numerical simulation. It is noted that the purpose of the present XFEM MITC plate element is to reproduce the locally non-smooth displacement by very few

elements. On the other hand, the locally non-smooth displacement can be reproduced by the FEM MITC formulation with a fine mesh without introducing enrichment. Hence, the usual concept of convergence in the standard FEM analysis is not applicable for the present XFEM MITC plate element.

In the meantime, in order to show the efficiency of the present XFEM formulation, comparisons on the computational costs for the three different types of analyses are listed in each example. The three types of analyses are: (i) the XFEM analyses with a coarse mesh, (ii) the standard FEM analyses with MITC6 triangular plate elements in a coarse mesh and (iii) the standard FEM analyses with a fine mesh. The computational cost includes the CPU time (t_{CPU}), the total number of DOF (n_{DOF}), the number of integration points (n_{IP}) and the times of stiffness matrix assemblage (n_s). All the analyses are conducted on a desktop with an Intel(R) Core(TM)2 Quad CPU Q9650 @3.00GHz. The generalized displacement control method [43] is employed as the solution technique in the numerical analyses and n_s is calculated based on the summation of the total incremental steps and the total iteration steps.

5.1 A flat plate with two fully fixed ends

A flat rectangular plate is tested in this example, as shown in Fig. 9. The length of the plate is L=5.0 and the width is b=1.0. The plate is fully fixed on the two short edges and free on the two long edges. The Young's modulus is $E=1\times10^6$, while the Poisson's ratio is υ=0.0. A coarse mesh which consists of 5 undistorted elements is used and the location of the three possible HGZs are shown in Fig. 10. In Fig. 10, the enriched nodes are indicated by the red dots and the green squares are the standard nodes. Five layers are used for each element in the thickness direction. In order to show the effectiveness of the MITC technique in the XFEM formulation, five cases with different thickness are tested. The yield strength of the material and the reference loading vary according to the thickness, as listed in Table 1, so that the ultimate loading factor λ_u are the same for all the five cases (λ_u = 0.625). The deflection of point A in Fig. 9 is investigated.

Firstly, an analysis on the XFEM formulation without the MITC technique in enriched elements is carried out in order to show the effects of shear locking in the XFEM plate elements. The analysis is based on a uniform coarse mesh, as shown in Fig. 10. In the analysis, the MITC technique is only applied to the standard elements, elements 3, 4, 7 and 8,

while the remaining elements, which are enriched elements, are compatible elements. The results from the XFEM analyses with thickness T1, T3 and T5 are shown in Fig. 11, together with the result from the MITC FEM analysis. It can be seen from Fig. 11 that the XFEM model is stiffer than the FEM model and the predicted ultimate loading from the XFEM formulation is even higher than that from the FEM formulation, which implies that shear locking appears in the enriched elements. Therefore, it is necessary to control shear locking in the XFEM plate elements. In the following analyses, the MITC technique is applied in both enriched and standard elements.

Secondly, an analysis with the MITC XFEM plate elements is conducted. The results obtained from a coarse ($1 \times 5 \times 2$ elements, the same as that for XFEM analysis) and a fine mesh ($10 \times 50 \times 2$ elements as shown in Fig. 12) are shown in Fig. 13, together with the result from the MITC XFEM elements. They are compared with the result from yield line pattern analysis [44] which gives an upper bound of the solution. It can be found in Fig. 13 that the XFEM formulation is able to capture the behavior of the flat plate in elasto-plastic analysis. The predicted ultimate loading factor λ_u obtained from XFEM formulation is close to that from the standard FEM with MITC6 triangular plate elements by using a fine mesh, which could be regarded as the limit of the Reissner-Mindlin plate theory. It can be seen from Fig. 13 that with the thickness decreases, the predicted ultimate loading factor does not shift a lot. This shows that the MITC6 scheme works well in shear locking mitigation in the present XFEM formulation in this example.

In addition, the effectiveness of the XFEM formulation in a distorted mesh is also shown in this example. The distorted mesh is shown in Fig. 14, from which it can be found that all the nodes are enriched. The result from the XFEM analysis with distorted mesh is shown in Fig. 15, comparing with the results from the uniform mesh XFEM analysis, the distorted and the uniform mesh FEM analyses.

The comparison on the total number of DOF and integration points is listed in Table 2. The initial load increment is λ_0=0.3 for all the three analyses. It could be seen that in the XFEM analysis with the uniform and the distorted mesh, much less DOF and integration points are used compared with the standard FEM analysis with the fine mesh.

5.2 An L-shape plate with two fully fixed ends

In this example, an L-shape plate with two fully fixed ends is tested (Fig. 16). Four cases with different thickness are tested to show the effectiveness of the MITC method in the shear locking control. The mesh scheme and the locations of three possible HGZs are shown in Fig. 17, in which the red dots represent the enriched nodes, the green square are the standard nodes and the blue triangles are the nodes enriched by two sets of additional DOF. The geometrical property is shown in Fig. 16. The Young's modulus is E=1.0×10^6, while the Poisson's ratio is υ=0.3. Again, the yield strength and the reference load are adjusted according to thickness (Table 3) so that the ultimate loadings for the four cases are the same (λ_u=3.0). Five layers are used for each element in the thickness direction. In this analysis, mesh pattern 1 is employed. The width of the HGZs in this example is chosen as l_{ns1}= l_{ns2} = 0.2 and l_{ns3}=0.6. The deflection of the corner point (point A in Fig. 16) is investigated.

Firstly, the analysis by the XFEM formulation without the MITC technique is conducted. The result is shown in Fig. 18 with the results from the XFEM MITC formulation and the standard FEM analysis by a coarse mesh. It can be seen from Fig. 18 that the XFEM formulation without the MITC technique locks seriously and the corresponding ultimate loading level is even higher than that from FEM analysis.

The results from the present XFEM MITC formulation are shown in Fig. 19 together with the result from the standard FEM by a coarse mesh (as shown in Fig. 17a) and by a fine mesh (1000 elements as shown in Fig. 17c). Besides, the result from a yield line pattern analysis is also shown in Fig. 19. It can be found from Fig. 19 that the MITC technique again preforms well in shear locking control in the present XFEM in this example.

In order to test the mesh-invariant of the present XFEM frame, mesh pattern 2 (Fig. 17b) is utilized in which the hypotenuses of the elements at the corner are perpendicular to the non-smoothness zone 3. The results from the standard FEM and the present XFEM formulation in pattern 2 with T1 case, together with the results from mesh pattern 1, are shown in Fig. 20. It can be seen that the results from the XFEM formulation in both mesh patterns are very close to each other, which implies that the present XFEM frame is mesh invariant.

The computational time of the four analyses, including the standard FEM analyses with the both coarse and fine meshes and the XFEM analyses with mesh pattern 1 and 2 are listed in Table 4. The initial loading factor λ_0 is 1.0 for all the four analyses. It can be seen from Table 4 that the computational time used in the XFEM analysis is much less than that of the fine meshed FEM analysis.

5.3 An L-shape cantilever plate

In this example, an L-shape cantilever plate is tested. The L-shape plate is fully fixed at one short edge and applied by a line load along the other short edge, as shown in Fig. 21. In order to verify the effectiveness of the MITC technique in controlling shear locking in the present XFEM formulation, a total of four cases with different thickness are tested. The geometrical property is shown in Fig. 21. The Young's modulus is E=1.0×10^6, while the Poisson's ratio is υ=0.3. As listed in Table 5, the yield strength of the material and the reference loading are normalized according to the thickness so that the ultimate loading factors from the four cases are the same (λ_u=0.9375). The mesh scheme, the locations and the width of the HGZ are shown in Fig. 22. The deflection of point A in Fig. 21 is investigated. The initial loading factor λ_0 is set as 0.3 for all the three types of analyses. The results from the present XFEM formulation are shown in Fig. 23 together with the results from the standard FEM by a coarse mesh (as shown in Fig. 22) and by a fine mesh (with 1000 MITC6 triangular plate elements as shown in Fig. 17c). The result obtained from the yield line pattern analysis [44] are also shown in Fig. 23 as reference.

It can be seen that the present XFEM formulation is able to capture the behavior of the L-shape plate in yield line analysis as good as the standard FEM analysis when the fine mesh is used. With the thickness decreases, the ultimate loading factor λ_u prediction remains virtually the same and the MITC technique again can mitigate shear locking in this example.

It can be seen that from Table 6, similar to the previous two examples, the total number of DOF and integration points used in this example are much less than those used in the standard FEM analysis with the fine mesh, while the total times of the stiffness matrix assemblage (n_s) for the three analyses are quite close to each other. In addition, the CPU time needed for the XFEM analysis is less than that for the FEM analysis with the fine mesh.

5.4 A square plate fixed at one edge

A square plate, with one edge fully fixed and a line load applied on the opposite edge, is tested in this example (in Fig. 24). The geometrical property is shown in Fig. 24. The Young's modulus is E =1.0×10^{10}. The Poisson's ratio is υ=0.2. The yield strength of the

material and the reference loading vary according to the thickness (Table 7) so that the ultimate loading factors from the four cases are the same (λ_u=0.25). For the coarse mesh, only 2 elements are used. The deflection of point A is investigated. The initial loading factor is λ_0=0.1 for all three types of analyses.

Firstly, the effectiveness of the MITC technique in circumventing shear locking in XFEM plate elements is demonstrated. With width of the HGZ is l_{ns}=4.0, the results from the present XFEM formulation are shown in Fig. 25. The results from the standard FEM by a coarse mesh (2 elements as the XFEM analysis) and by a fine mesh (20 × 20 ×2 MITC6 triangular plate elements) and from the yield line pattern analysis [44] are also shown in Fig. 25 for comparison. From Fig. 25, it can be easily seen that the XFEM formulation improves the accuracy of the ultimate loading prediction a lot when comparing with the standard FEM analysis with the same mesh. Again, the MITC technique performs well in this example. It can be seen from Fig. 26 that the XFEM formulation locks if the MITC technique is not applied on the enriched displacement field.

Secondly, an analysis is carried out to study the influence from the width of non-smoothness zone l_{ns} on the numerical results. The value l_{ns} is taken as 1.0, 2.0, 4.0, 6.0 and 8.0. The results are shown in Fig. 27. It can be seen from Fig. 27 that the predicted ultimate loading level λ_u from l_{ns} =1.0, 2.0 and 4.0 are quite close to each other, while the ultimate loading level is higher with a wider width of the non-smoothness zone when l_{ns} is greater than 4.0. This phenomenon can be explained as the following: when the width l_{ns} is large, the gradient of the non-smooth part in the enrichment function is reduced and the XFEM formulation fails to capture the locally non-smooth displacement.

The comparison on the computational effort of the three types of analyses is listed in Table 8. Obviously, the DOF and integration points used in the XFEM analysis are much less than those employed in the standard FEM analysis with the fine mesh. As a result, the computational time of the XFEM analysis is less than that of the fine meshed FEM analysis. However, the numerical results from the two analyses are quite close to each other.

In this example, the important of using the MITC scheme in the XFEM formulation is studied. Four cases are conducted: the XFEM MITC formulation (i.e. the XFEM with SaEa formulation, Eqn (17)), the XFEM with ScEa formulation (Eqn (24)), the XFEM with SaEc formulation (Eqn (25)) and the XFEM formulation with compatible shear strain field (i.e. the XFEM with ScEc formulation or totally no shear locking control). The results are shown in

Fig. 28. It can be seen that when the shear strain corresponding to the standard displacement field is compatible, the XFEM formulations (the XFEM with ScEa formulation and the XFEM with ScEc formulation) fail to improve the prediction of the ultimate loading and the results are even worse than that from the FEM MITC elements. When the MITC technique is applied on the standard displacement field, the XFEM formulation is able to improve the numerical results. Furthermore, a much better result can be obtained by applying the MITC technique in both standard and enriched fields.

6 Conclusions

In this paper, a 6-node triangular XFEM plate element with MITC technique is presented. The enrichment used in the XFEM plate element is able to model a high gradient zone in displacement fields resulted from yield lines. The enrichments are constructed on the structure level so that they are independent of the physical shape of the enriched element. Regularized enrichments are used for both rotation and deflection displacement approximation fields so that the enrichment can be activated automatically. As the relationship between the appearance of the non-smooth displacement and the appearance of a yield line is not clear, the employment of the regularized enrichment makes it easy to use the XFEM formulation in yield line analyses. The MITC technique is adopted to circumvent shear locking in both smooth and non-smooth transverse shear strain field. An alternative expression of the MITC6 scheme which directly relates the assumed shear strain components with the nodal displacement variables is derived. The alternative expression, which is equivalent to the original form, could be easily used in conjunction with the present XFEM formulation. It is shown in the numerical examples that shear locking appears in both standard and enriched displacement field and the MITC6 scheme is able to control shear locking effectively in enriched elements.

Although the present XFEM formulation shows its effectiveness in capture the behavior of plate structures in elasto-plastic analyses, it is premature to state that the enrichment function presented in this article is the best choice for the high gradient zone resulted from yield lines. Since the shape and the area of a high gradient zone depends on a few factors such as the cross-sectional shape of the plate, the loading and support boundary conditions, a further study on choosing more optimal enrichment functions could be a research topic in future.

Besides, the application of the present XFEM formulation in large deformation analysis could be studied in future research.

Reference

[1] Zienkiewicz OC, Taylor RL. Finite Element Method for Solid and Structural Mechanics (6th Edition). Elsevier; 2005.
[2] Bathe K-J, Dvorkin EN. A four-node plate bending element based on Mindlin/Reissner plate theory and a mixed interpolation. International Journal for Numerical Methods in Engineering. 1985;21:367-83.
[3] Bathe K-J, Brezzi F, Cho SW. The MITC7 and MITC9 Plate bending elements. Computers & Structures. 1989;32:797-814.
[4] Bathe K-J. Finite Element Procedures. 2 ed. New Jersey: Prentice Hall; 1995.
[5] Eduardo ND, Klaus-Jürgen B. A continuum mechanics based four-node shell element for general non-linear analysis. Engineering Computations. 1984;1:77-88.
[6] Bathe K-J, Dvorkin EN. A formulation of general shell elements—the use of mixed interpolation of tensorial components. International Journal for Numerical Methods in Engineering. 1986;22:697-722.
[7] Bucalem ML, Bathe K-J. Higher-order MITC general shell elements. International Journal for Numerical Methods in Engineering. 1993;36:3729-54.
[8] Bucalem ML, Shimura da Nóbrega SH. A mixed formulation for general triangular isoparametric shell elements based on the degenerated solid approach. Computers & Structures. 2000;78:35-44.
[9] Lee P-S, Bathe K-J. Development of MITC isotropic triangular shell finite elements. Computers & Structures. 2004;82:945-62.
[10] Dominique Chapelle, Klaus-Jurgen Bathe. The finite element analysis of shells – fundamentals. 2 ed: Springer-Verlag; 2011.
[11] Lee PS, Bathe KJ. The quadratic MITC plate and MITC shell elements in plate bending. Advances in Engineering Software. 2010;41:712-28.
[12] Beirão da Veiga L, Chapelle D, Paris Suarez I. Towards improving the MITC6 triangular shell element. Computers & Structures. 2007;85:1589-610.
[13] Kim DN, Bathe KJ. A triangular six-node shell element. Computers & Structures. 2009;87:1451-60.
[14] Bathe K-J, Lee P-S, Hiller J-F. Towards improving the MITC9 shell element. Computers & Structures. 2003;81:477-89.
[15] Lee Y, Yoon K, Lee PS. Improving the MITC3 shell finite element by using the Hellinger-Reissner principle. Computers & Structures. 2012;110:93-106.
[16] Lee P-S, Noh H-C, Bathe K-J. Insight into 3-node triangular shell finite elements: the effects of element isotropy and mesh patterns. Computers & Structures. 2007;85:404-18.
[17] Bathe KJ, Brezzi F, Marini LD. The MITC9 shell element in plate bending: mathematical analysis of a simplified case. Computational Mechanics. 2011;47:617-26.
[18] Nguyen-Thanh N, Rabczuk T, Nguyen-Xuan H, Bordas SPA. A smoothed finite element method for shell analysis. Computer Methods in Applied Mechanics and Engineering. 2008;198:165-77.
[19] Carrera E, Cinefra M, Nali P. MITC technique extended to variable kinematic multilayered plate elements. Composite Structures. 2010;92:1888-95.

[20] Xu J, Lee CK, Tan KH. An XFEM plate element for high gradient zones resulted from yield lines. International Journal for Numerical Methods in Engineering. 2013;93:1314-44.
[21] Xu J, Lee CK, Tan KH. An XFEM frame for plate elements in yield line analyses. Accepted for publication by the International Journal for Numerical Methods in Engineering. in press.
[22] Xu J, Lee CK, Tan KH. A two-dimensional co-rotational Timoshenko beam element with XFEM formulation. Computational Mechanics. 2012;49:667-83.
[23] Patzák B, Jirásek M. Process zone resolution by extended finite elements. Engineering Fracture Mechanics. 2003;70:957-77.
[24] Areias PMA, Belytschko T. Two-scale shear band evolution by local partition of unity. International Journal for Numerical Methods in Engineering. 2006;66:878-910.
[25] Benvenuti E, Tralli A, Ventura G. A regularized XFEM model for the transition from continuous to discontinuous displacements. International Journal for Numerical Methods in Engineering. 2008;74:911-44.
[26] Benvenuti E. A regularized XFEM framework for embedded cohesive interfaces. Computer Methods in Applied Mechanics and Engineering. 2008;197:4367-78.
[27] Belytschko T, Gracie R. On XFEM applications to dislocations and interfaces. International Journal of Plasticity. 2007;23:1721-38.
[28] Belytschko T, Black T. Elastic crack growth in finite elements with minimal remeshing. International Journal for Numerical Methods in Engineering. 1999;45:601-20.
[29] Moës N, Dolbow J, Belytschko T. A finite element method for crack growth without remeshing. International Journal for Numerical Methods in Engineering. 1999;46:131-50.
[30] Sukumar N, Chopp DL, Moës N, Belytschko T. Modeling holes and inclusions by level sets in the extended finite-element method. Computer Methods in Applied Mechanics and Engineering. 2001;190:6183-200.
[31] Moës N, Cloirec M, Cartraud P, Remacle JF. A computational approach to handle complex microstructure geometries. Computer Methods in Applied Mechanics and Engineering. 2003;192:3163-77.
[32] Zi G, Belytschko T. New crack-tip elements for XFEM and applications to cohesive cracks. International Journal for Numerical Methods in Engineering. 2003;57:2221-40.
[33] Areias PMA, Belytschko T. Non-linear analysis of shells with arbitrary evolving cracks using XFEM. International Journal for Numerical Methods in Engineering. 2005;62:384-415.
[34] Areias PMA, Belytschko T. Analysis of three-dimensional crack initiation and propagation using the extended finite element method. International Journal for Numerical Methods in Engineering. 2005;63:760-88.
[35] Stazi FL, Budyn E, Chessa J, Belytschko T. An extended finite element method with higher-order elements for curved cracks. Computational Mechanics. 2003;31:38-48.
[36] Fries T-P. A corrected XFEM approximation without problems in blending elements. International Journal for Numerical Methods in Engineering. 2008;75:503-32.
[37] Fries T-P, Belytschko T. The extended/generalized finite element method: An overview of the method and its applications. International Journal for Numerical Methods in Engineering. 2010;84:253-304.
[38] Gracie R, Wang H, Belytschko T. Blending in the extended finite element method by discontinuous Galerkin and assumed strain methods. International Journal for Numerical Methods in Engineering. 2008;74:1645-69.
[39] Abbas S, Alizada A, Fries TP. The XFEM for high-gradient solutions in convection-dominated problems. International Journal for Numerical Methods in Engineering. 2010;82:1044-72.
[40] Crisfield MA. Non-Linear Finite Element Analysis of Solids and Structures, Volume 2, Advanced topics. 1 ed. Chichester: John Wiley & Sons; 1991.

[41] Zienkiewicz OC, Taylor RL. Finite Element Method (5th Edition) Volume 2 - Solid Mechanics. Elsevier; 2000.
[42] Simo JC, Hughes TJR. Computational Inelasticity. Springer New York; 1998. p. 113-53.
[43] Yang YB, Shieh MS. Solution method for nonlinear problems with multiple critical points. AIAA Journal. 1990;28:2110-6.
[44] Johansen KW. Yield-line formulae for slabs: Taylor & Francis; 1972.

Totally, 29 figures and 8 tables

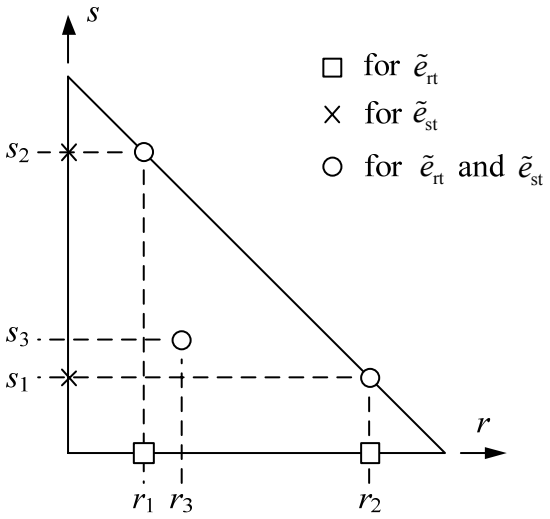

(a) locations of the tying points in the MITC6 scheme

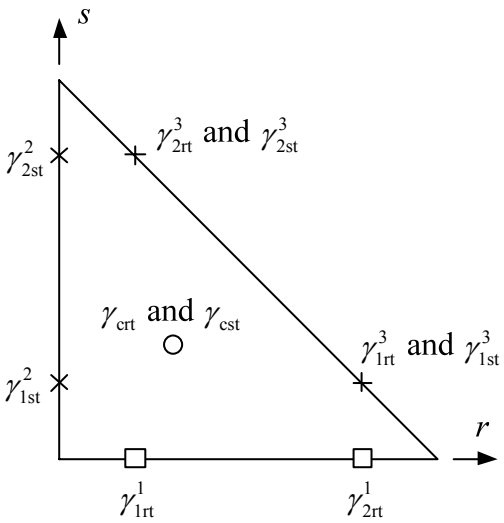

(b) compatible shear strain components used in the tying points

Fig. 1 The tying points in the MITC6 scheme

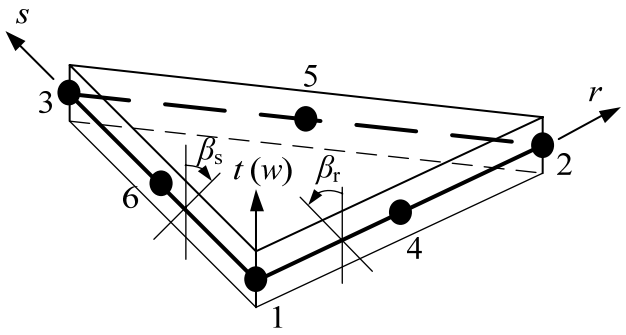

Fig. 2 The local coordinate system for the plate elements

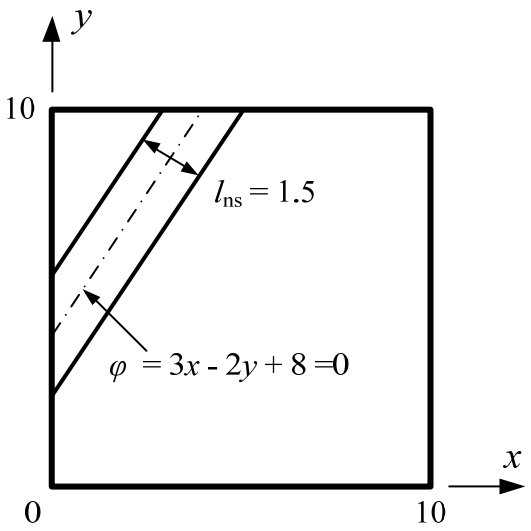

Fig. 3 An example of HGZ

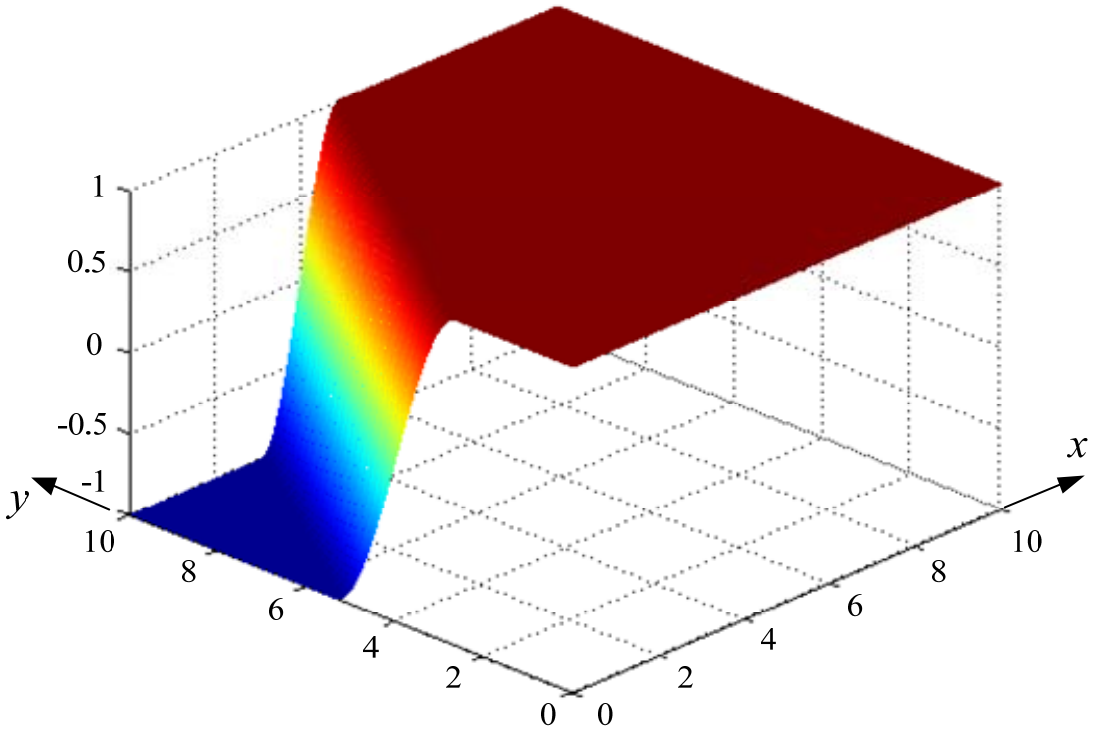

(a) 3D plot of R

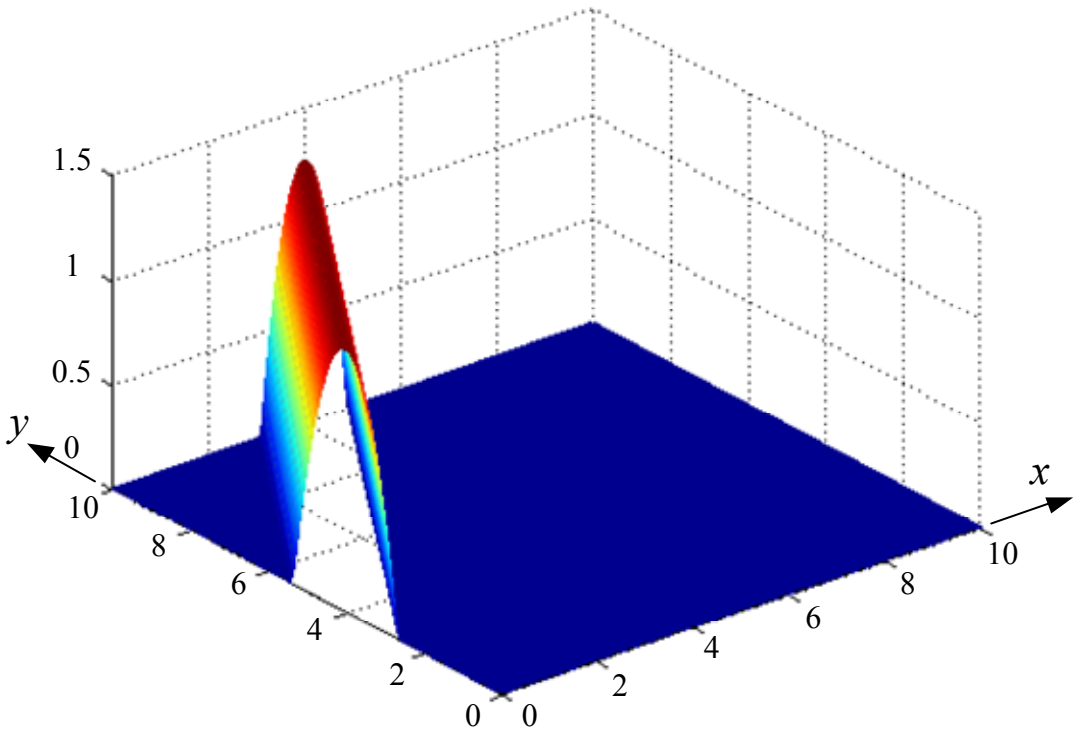

(b) 3D plot of $\partial R/\partial x$

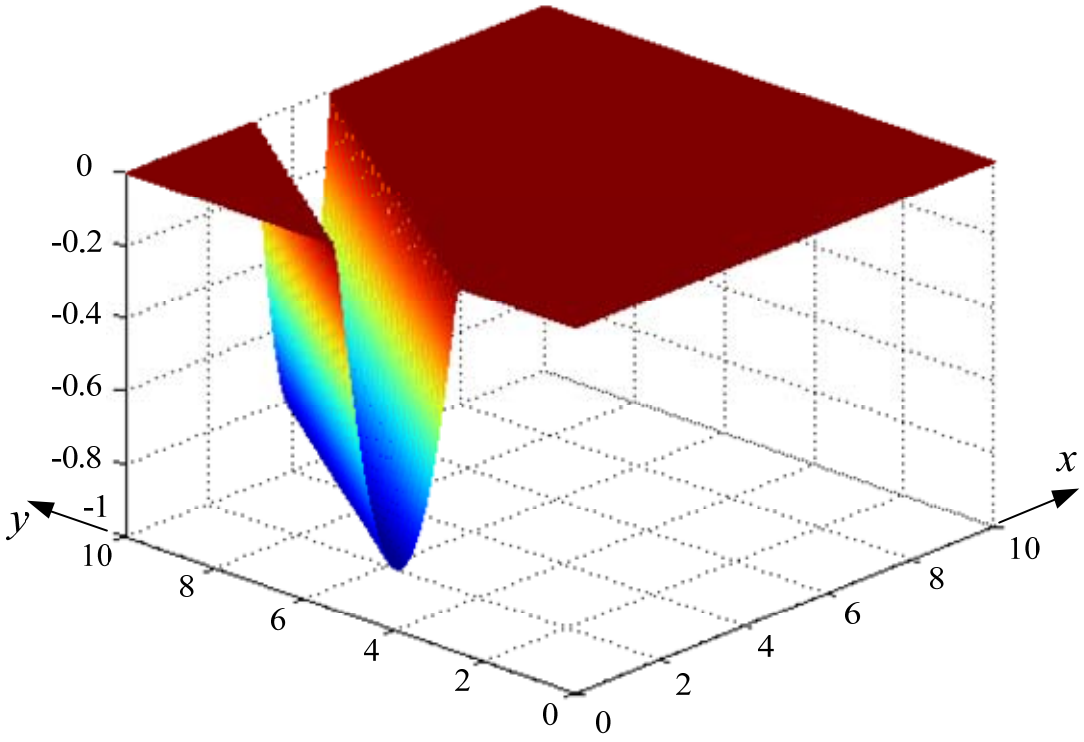

(c) 3D plot of $\partial R/\partial y$

Fig. 4 Plots of R and its first derivative with respect to the global coordinates

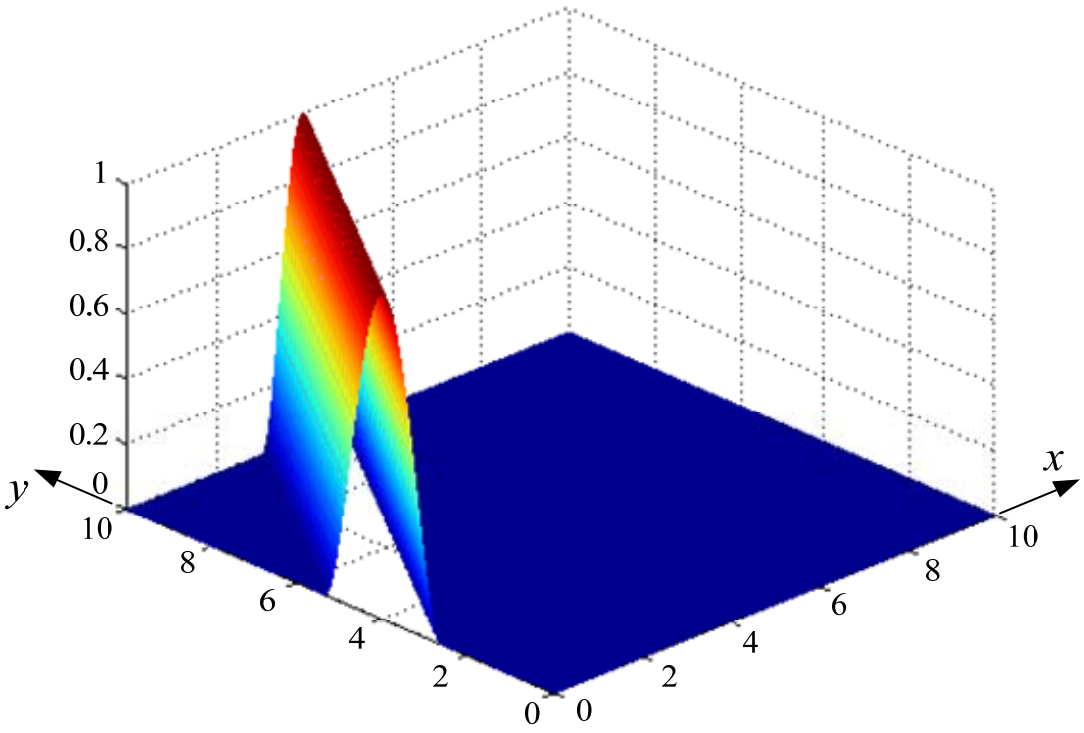

(a) 3D plot of F

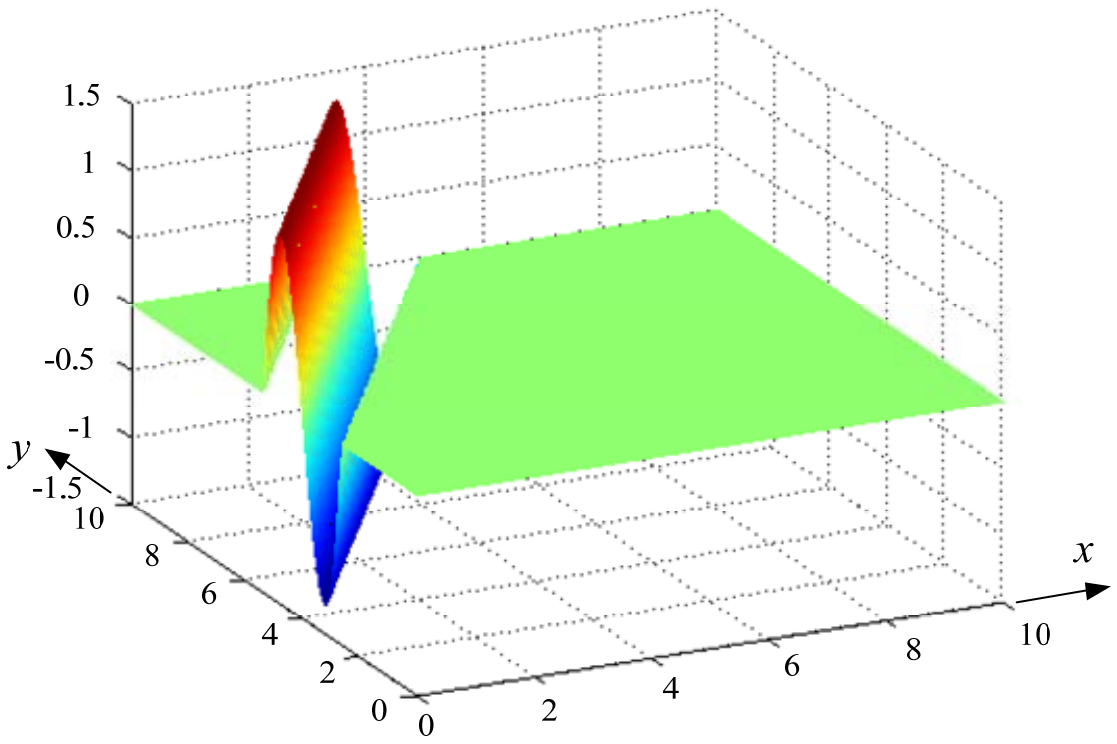

(b) 3D plot of $\partial F/\partial x$

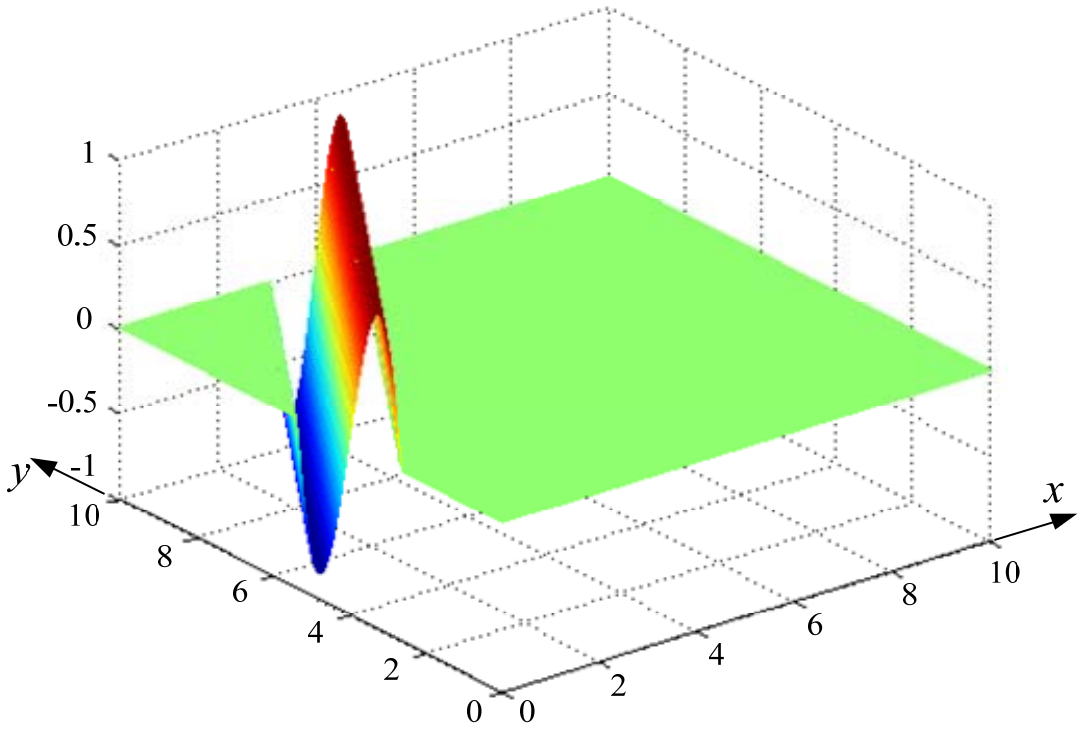

(c) 3D plot of $\partial F/\partial y$

Fig. 5 Plots of F and its first derivative with respect to the global coordinates

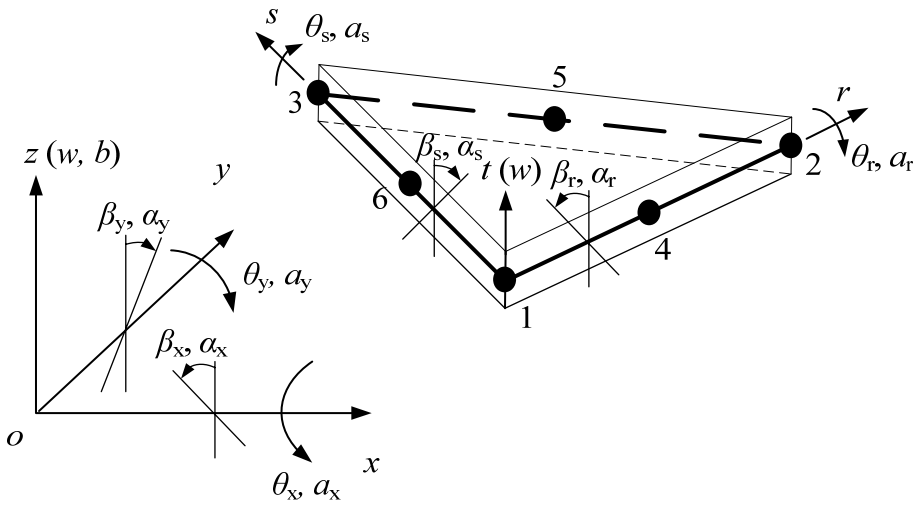

Fig. 6 DOF and natural coordinate system of an enriched element

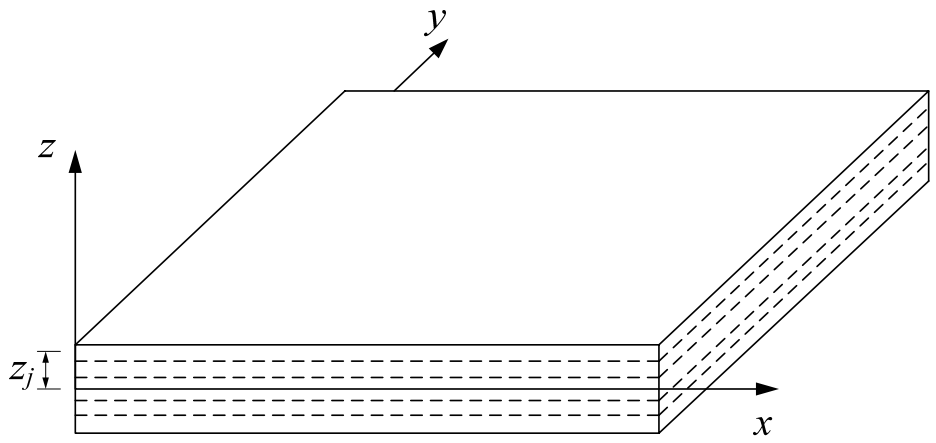

Fig. 7 The layered model

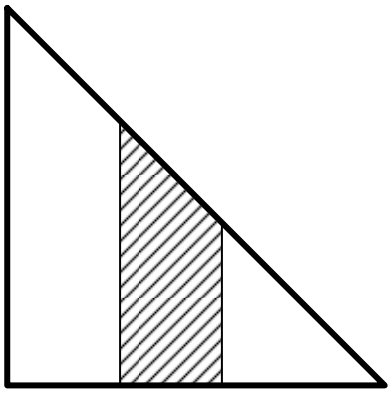

(a) 1 QU_H + 1 QU_nH + 1 TR_nH

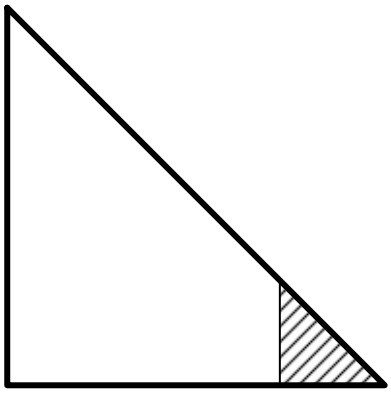

(b) 1 TR_H + 1 QU_nH

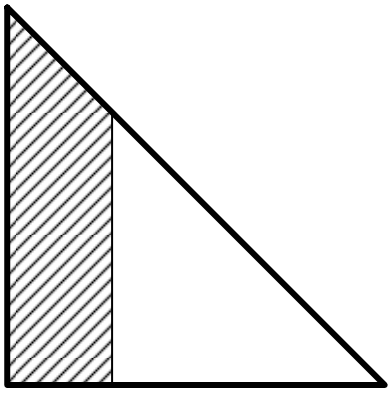

(c) 1 QU_H + 1 TR_nH

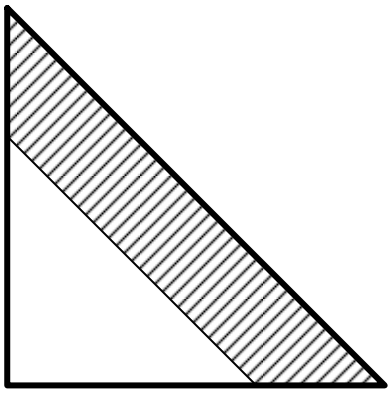

(d) 1 QU_H + 1 TR_nH

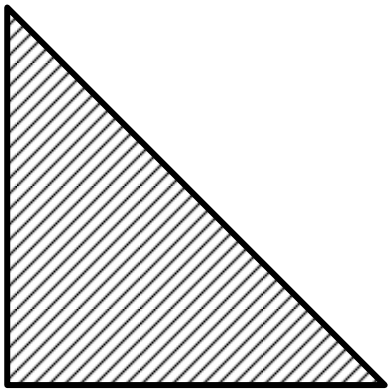

(e) 1 TR_H

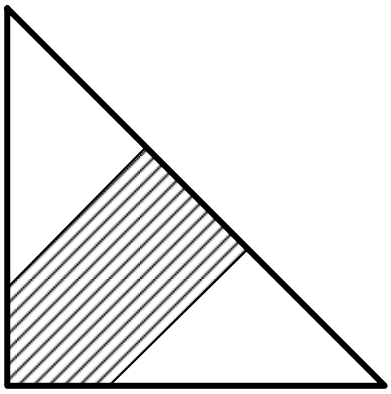

(f) 1 PE_H + 2 TR_nH

Fig. 8 Possible partitions of an enriched element

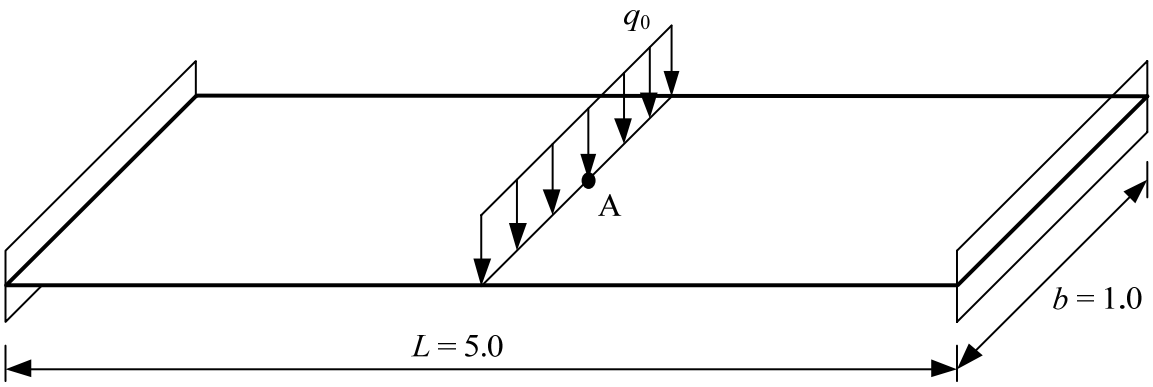

Fig. 9 A flat strip with two fully fixed ends

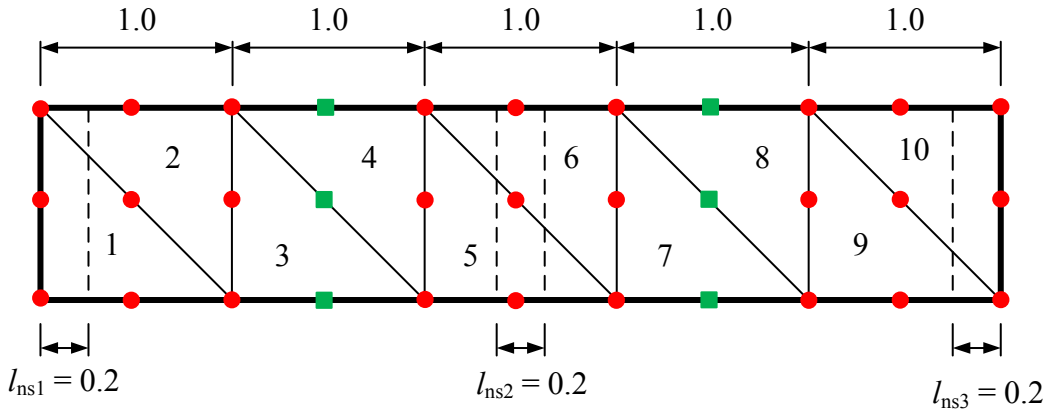

Fig. 10 The uniform mesh used for the flat strip problem (red dots: enriched nodes; green squares: standard nodes)

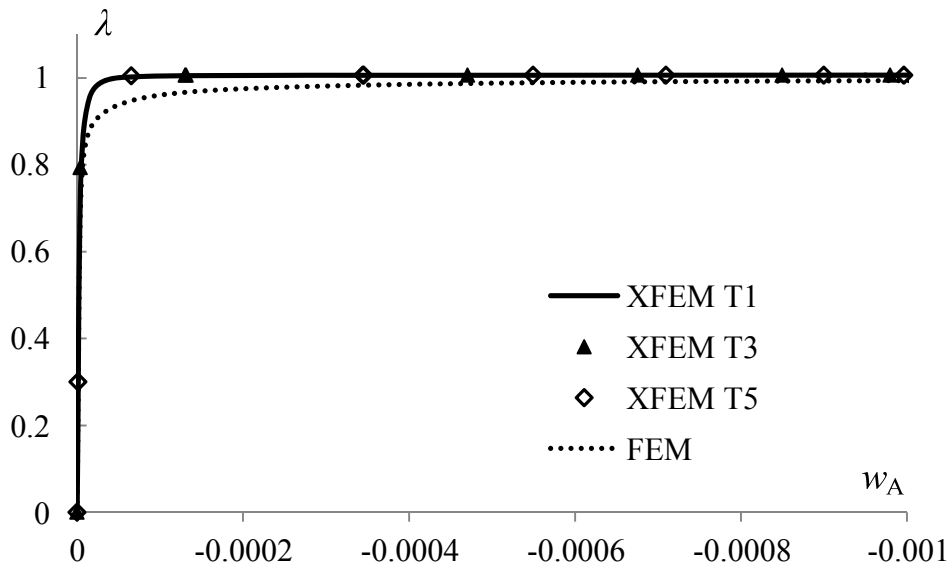

Fig. 11 The equilibrium paths of the flat strip problem without the MITC scheme in enriched element

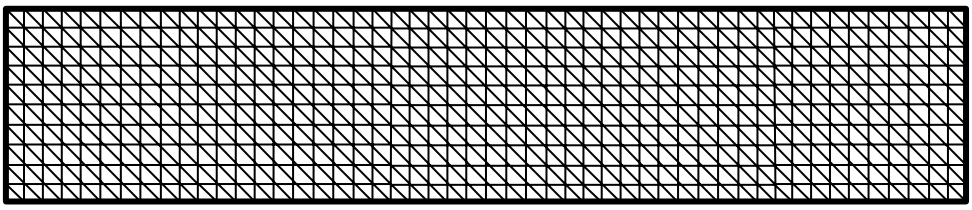

Fig. 12 The fine mesh for FEM analysis for the flat strip problem.

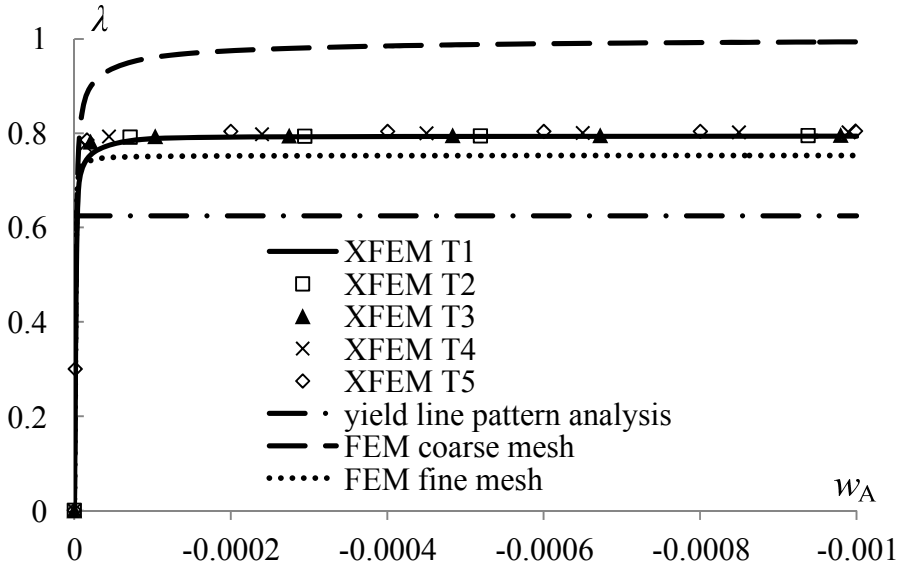

Fig. 13 The equilibrium paths of the flat strip problem with uniform mesh

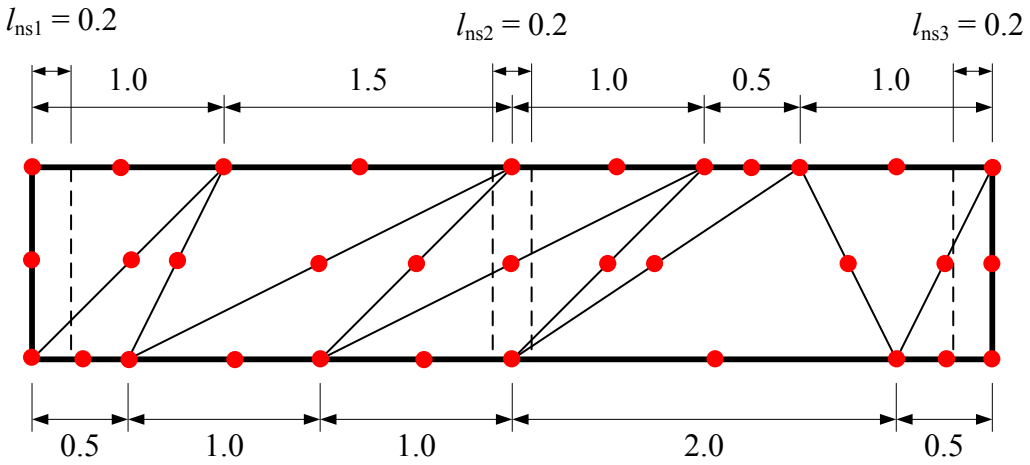

Fig. 14 The distorted mesh for the flat strip problem (all nodes are enriched)

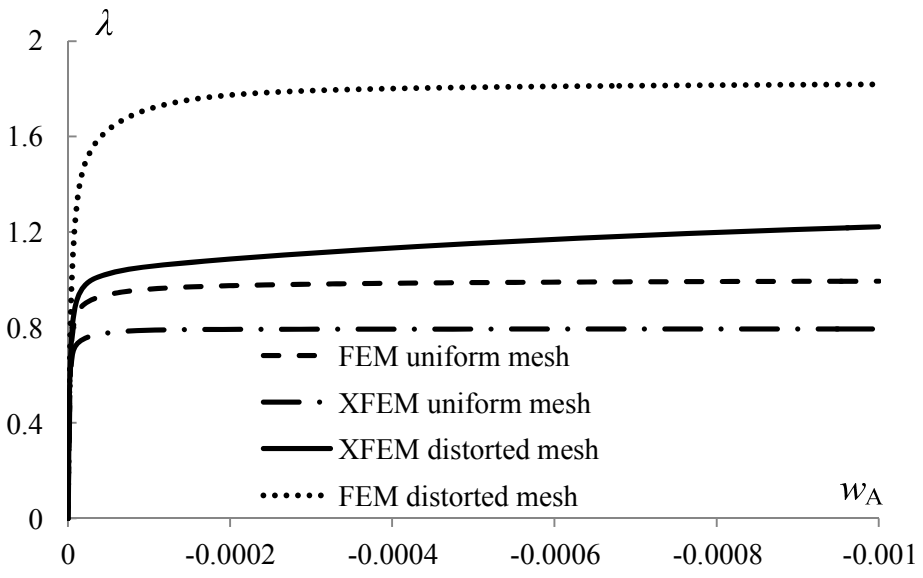

Fig. 15 The comparison of results obtained from uniform mesh and distorted mesh for the flat strip problem

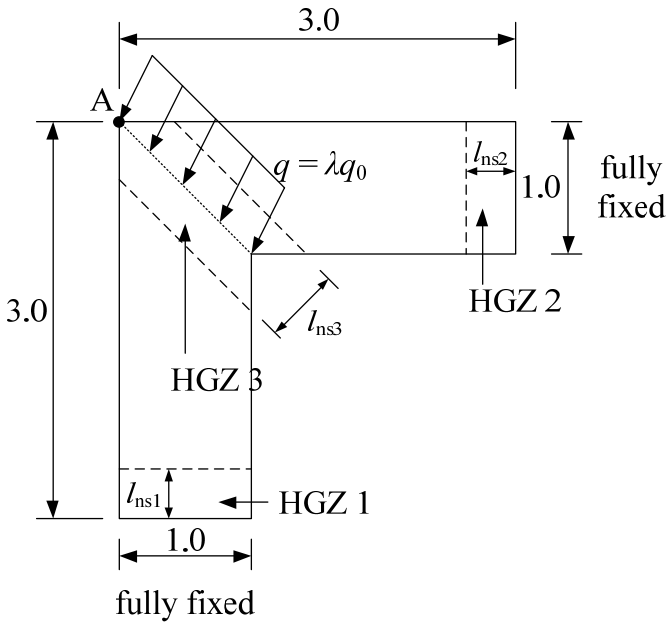

Fig. 16 An L-shape plate fixed on the two short edges

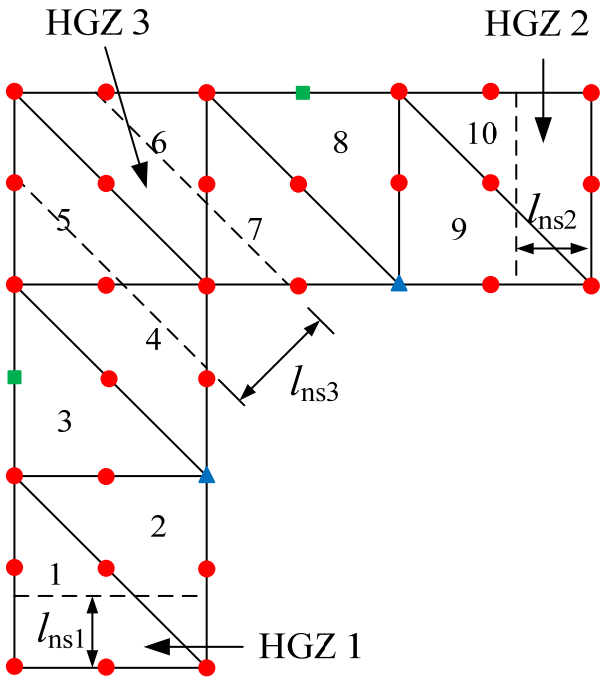

(a) Mesh pattern 1

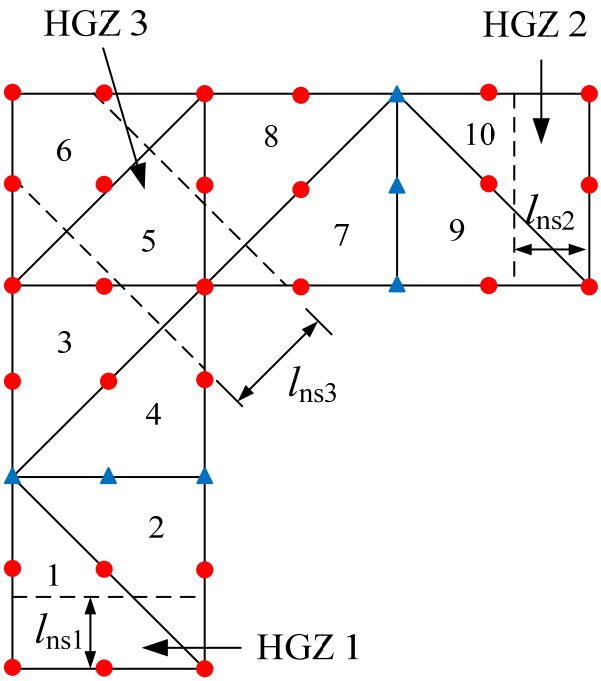

(b) Mesh pattern 2

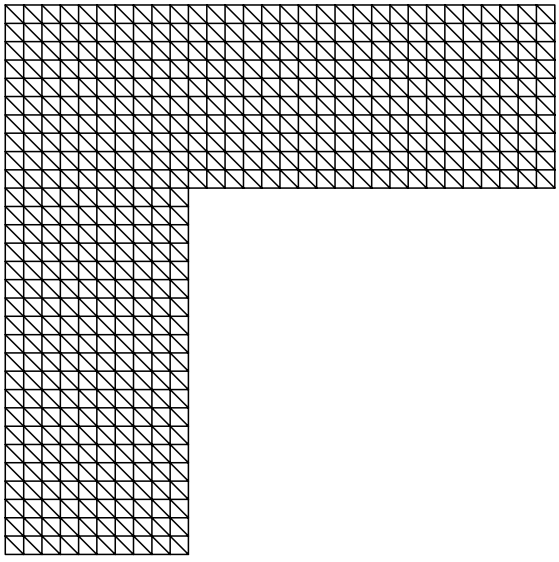

(c) fine mesh for FEM analysis

Fig. 17 The mesh schemes of the L-shape plate problem (red dots: enriched nodes; green squares: standard nodes and blue triangles: nodes enriched by two sets of additional DOF)

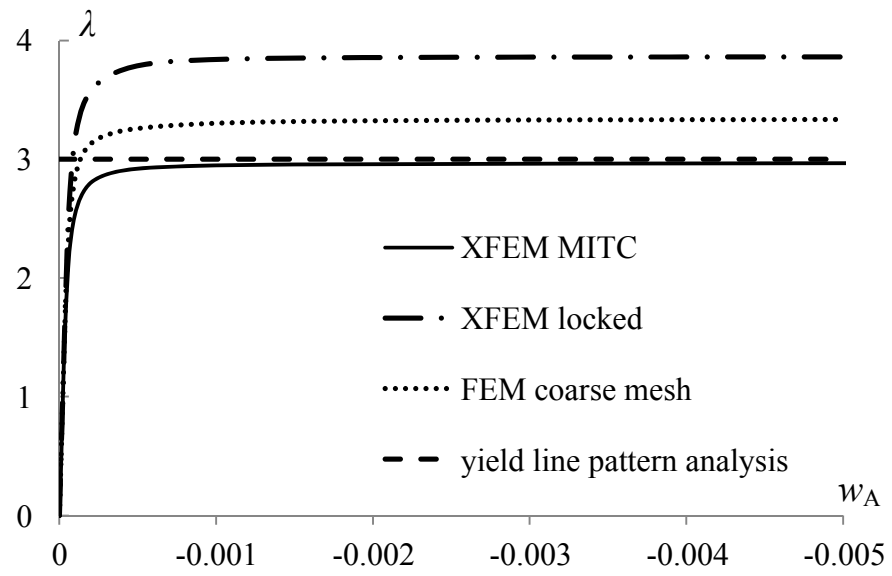

Fig. 18 The equilibrium paths for the L-shape plate problem with shear locking in XFEM formulation

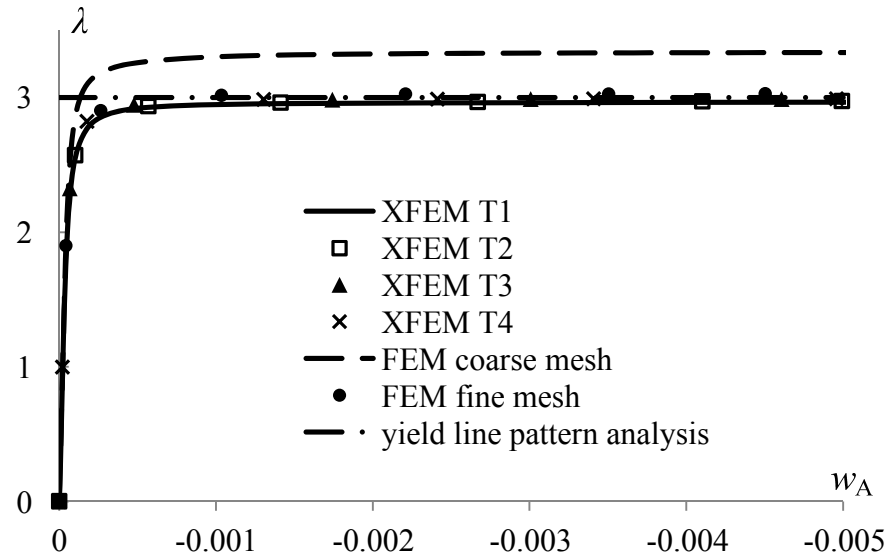

Fig. 19 The equilibrium paths of the L-shape plate problem (different thickness)

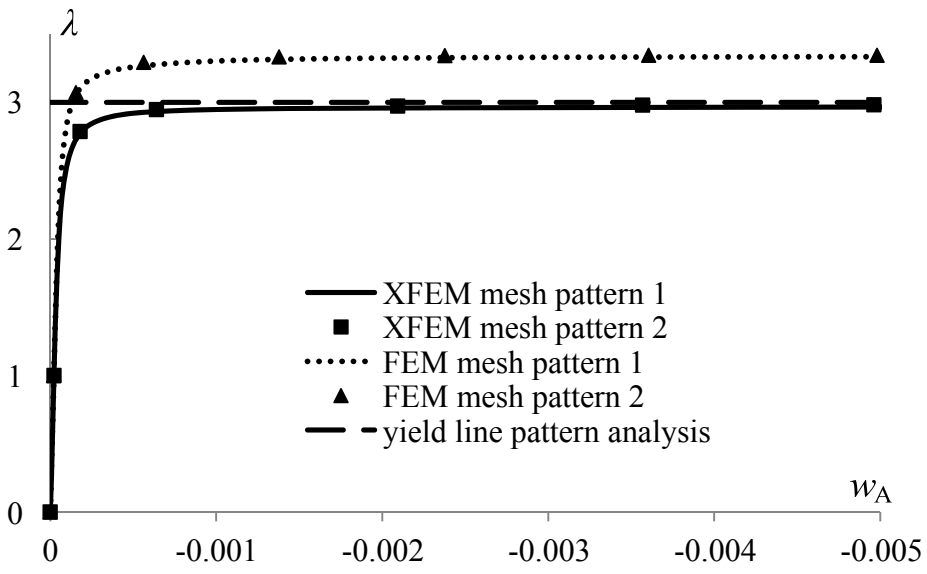

Fig. 20 The equilibrium paths of the L-shape plate problem (different mesh patterns)

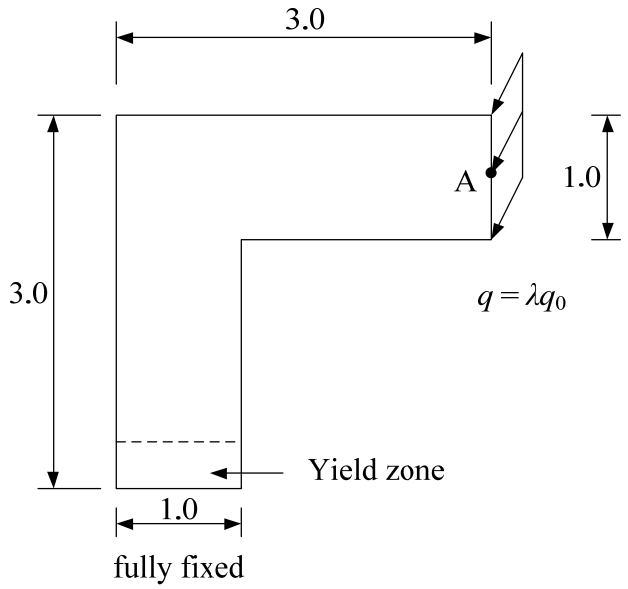

Fig. 21 An L-shape cantilever plate

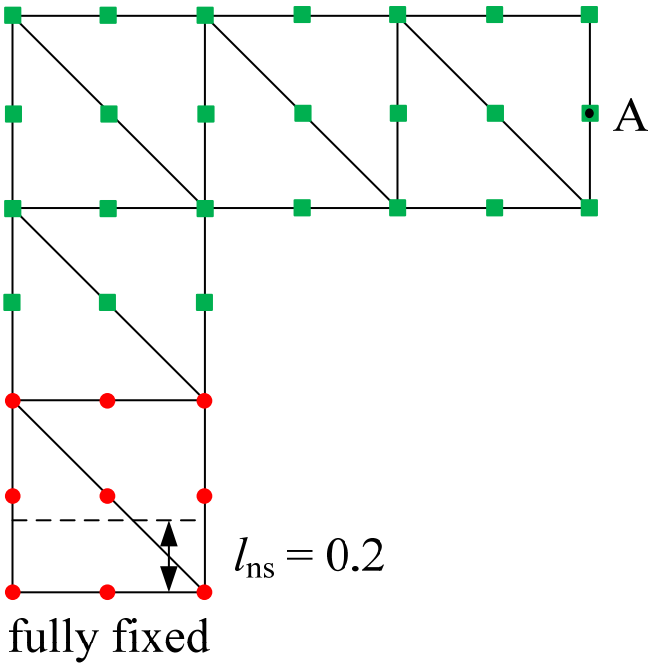

Fig. 22 The mesh pattern of the L-shape cantilever plate problem (red dots: enriched nodes and green squares: standard nodes)

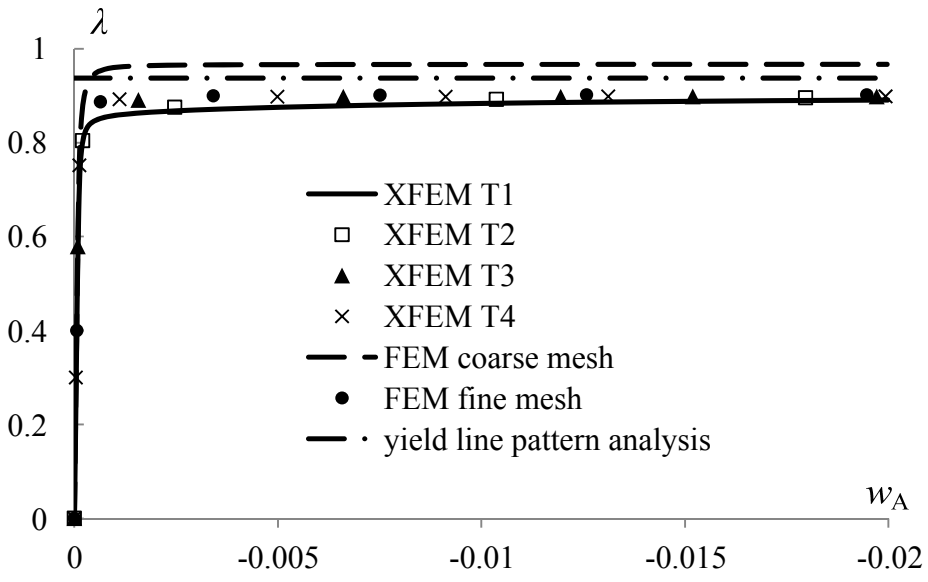

Fig. 23 The equilibrium paths of the L-shape cantilever plate problem

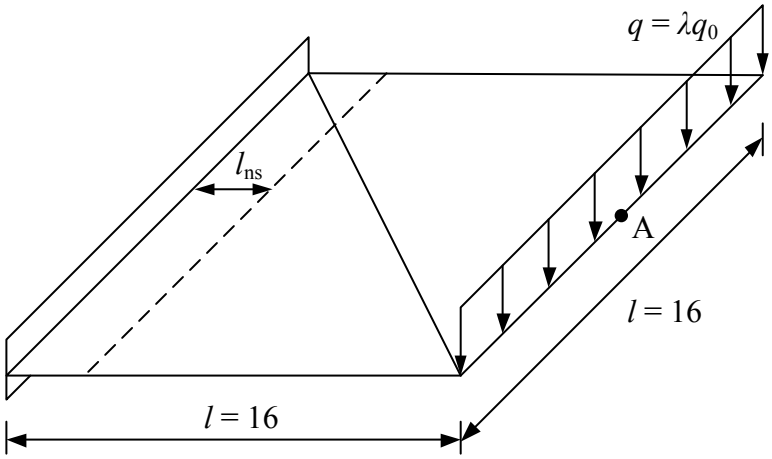

(a) loading, boundary conditions and the coarse mesh

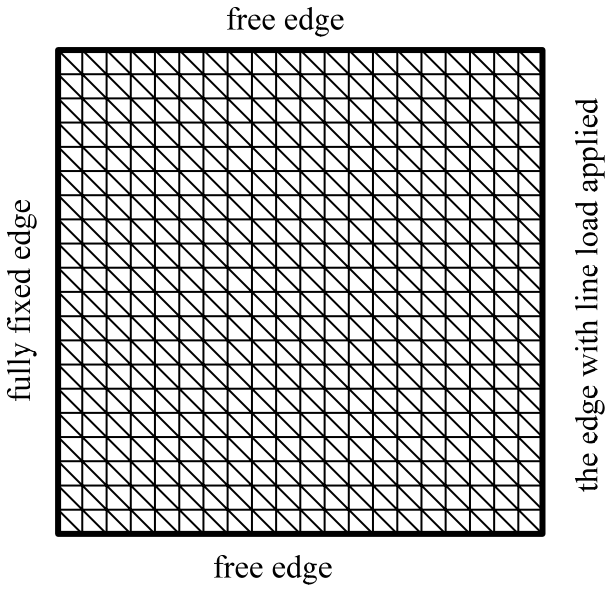

(b) fine FEM mesh

Fig. 24 A square plate fixed at one edge and applied by a line load at the opposite edge

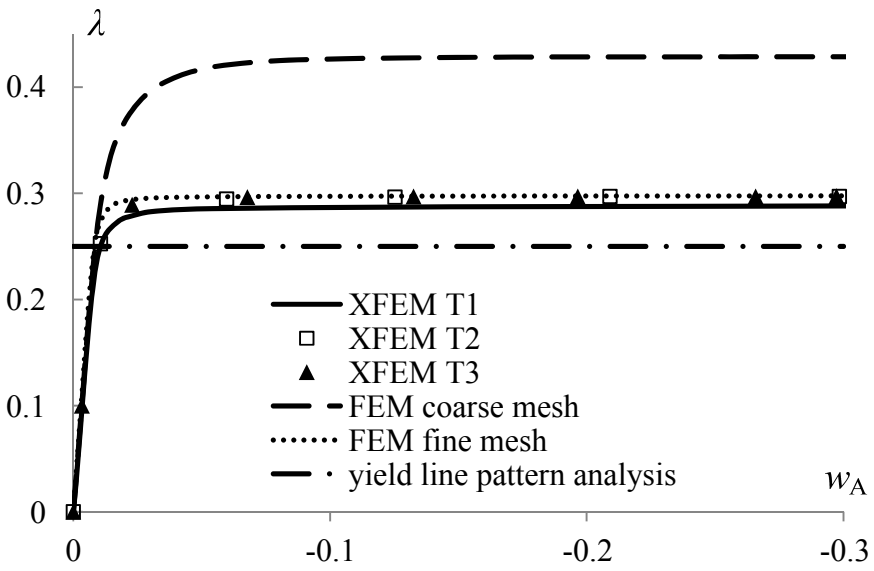

Fig. 25 The equilibrium paths of the square plate problem

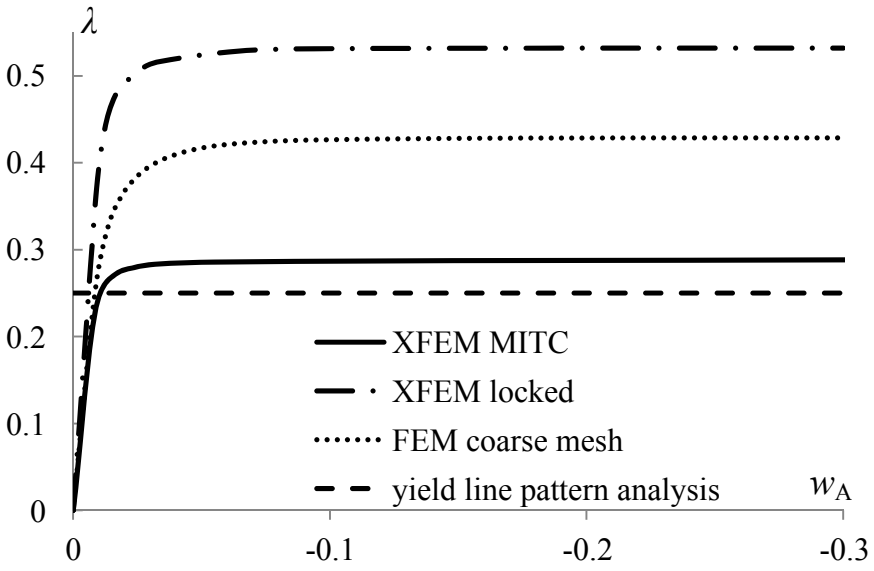

Fig. 26 The equilibrium paths of the square plate problem with shear locking

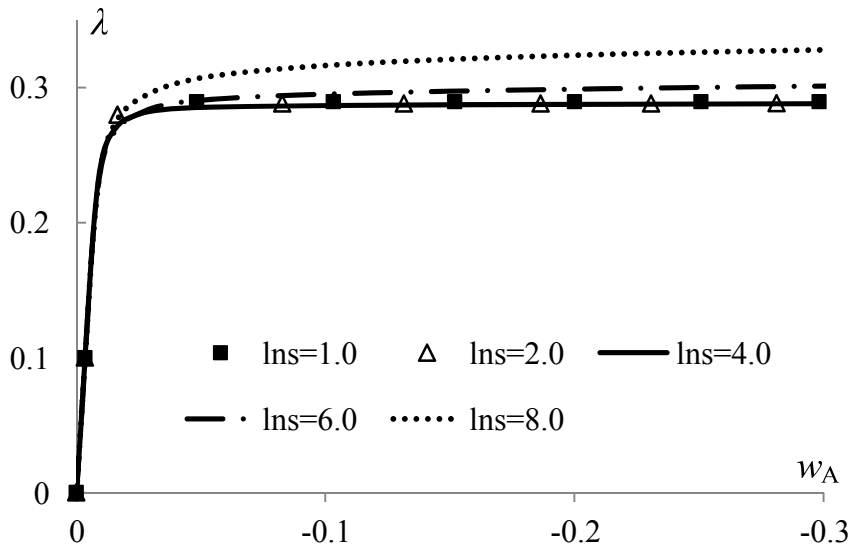

Fig. 27 The equilibrium paths of the square plate problem with different l_{ns}

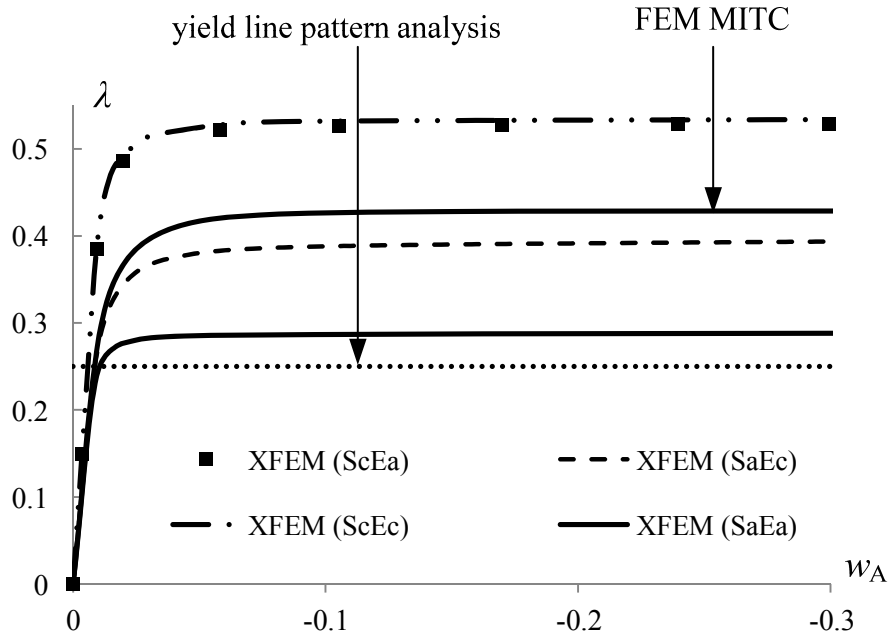

Fig. 28 The equilibrium paths of the square plate problem from the analyses with different assumed strain interpolation

Table 1 A flat strip with five different plate thicknesses

	thickness t	yield strength σ_y	reference loading q_0	thickness/length ratio t / L
T1	0.5	0.4	6.4×10^{-2}	1 / 10
T2	0.25	0.2	8×10^{-3}	1 / 20
T3	0.125	0.1	1×10^{-3}	1 / 40
T4	0.05	0.04	6.4×10^{-5}	1 / 100
T5	0.01	0.008	5.12×10^{-7}	1 / 500

Table 2 Comparison of the DOF and integration points for the flat strip problem

	n_{uen}	n_{en}	n_{DOF}	n_{IP}	n_s	t_{CPU} (second)
FEM coarse mesh	33	0	99	30×5=150	735	50.2
FEM fine mesh	2121	0	6363	3,000×5=15,000	798	7063.3
XFEM uniform mesh	6	27	180	516×5=2,580	735	1091

Table 3 An L-shape plate with four different plate thicknesses

	thickness t	yield strength σ_y	reference loading q_0
T1	0.15	1.0	-2.12×10^{-3}
T2	0.1	6.67×10^{-1}	-6.29×10^{-4}
T3	0.03	0.2	-1.70×10^{-5}
T4	0.01	6.67×10^{-2}	-6.29×10^{-7}

Table 4 Comparison of the DOF and integration points for the L-shape plate problem

	n_{uen}	n_{en}	n_{DOF}	n_{IP}	n_s	t_{CPU} (second)
FEM coarse mesh	33	0	99	30×5=150	269	17.3
FEM fine mesh	2121	0	6363	3,000×5=15,000	286	1965.2
XFEM mesh pattern 1	6	27	180	582×5=2,910	271	477.2

Table 5 An L-shape cantilever plate with four different plate thicknesses

	thickness t	yield strength σ_0	reference load q_0
T1	0.15	1	2.40×10^{-3}
T2	0.1	0.667	7.11×10^{-4}
T3	0.03	0.2	1.92×10^{-5}
T4	0.01	0.06667	7.11×10^{-7}

Table 6 Comparison of the DOF and integration points for the L-shape cantilever plate problem

	n_{uen}	n_{en}	n_{DOF}	n_{IP}	n_s	t_{CPU} (second)
FEM coarse	33	0	99	30×5=150	554	37.1
FEM fine mesh	2121	0	6363	3,000×5=15,000	515	3593.9
XFEM	24	9	126	168×5=840	570	273.4

Table 7 A square plate with three different plate thicknesses

	thickness t	yield strength σ_0	reference load q_0	thickness to length ratio t / L
T1	1	3.0×10^5	3.0×10^5	1 / 16
T2	0.1	3.0×10^4	300	1 / 160
T3	0.01	3.0×10^3	0.3	1 / 1600

Table 8 Comparison of the computational cost for the square plate problem

	n_{uen}	n_{en}	n_{DOF}	n_{IP}	n_{s}	t_{CPU} (second)
FEM coarse mesh (1 × 1 × 2)	9	0	27	6×5=30	133	1.6
FEM fine mesh (20 × 20 × 2)	1681	0	5043	2,400×5=12,000	129	672.6
XFEM (1 × 1 × 2)	0	9	54	144×5=720	110	42.2